THERMAL INSTABILITIES AND POLOIDAL ASYMMETRIES IN THE TOKAMAK EDGE PLASMA

J. Neuhauser, W. Schneider, R. Wunderlich

IPP 5/8 December 1985

MAX-PLANCK-INSTITUT FÜR PLASMAPHYSIK

8046 GARCHING BEI MÜNCHEN

MAX-PLANCK-INSTITUT FÜR PLASMAPHYSIK

GARCHING BEI MÜNCHEN

THERMAL INSTABILITIES AND POLOIDAL ASYMMETRIES IN THE TOKAMAK EDGE PLASMA

J. Neuhauser, W. Schneider, R. Wunderlich

IPP 5/8 December 1985

Die nachstehende Arbeit wurde im Rahmen des Vertrages zwischen dem Max-Planck-Institut für Plasmaphysik und der Europäischen Atomgemeinschaft über die Zusammenarbeit auf dem Gebiete der Plasmaphysik durchgeführt.

THERMAL INSTABILITIES AND POLOIDAL ASYMMETRIES IN THE TOKAMAK EDGE PLASMA

J. Neuhauser, W. Schneider, R. Wunderlich

IPP 5/8

Abstract

The thermal stability of a collisional, radiating edge plasma of magnetic confinement experiments is investigated analytically and numerically. A fluid description is used including a non-local electron heat flux model and non-equilibrium impurity radiation cooling. The dispersion relation of a homogeneous plasma is derived analytically and stability criteria are given. Various experimental scenarios are simulated with a sophisticated numerical model, demonstrating the formation and history of global and local "marfes" and relaxation oscillations under appropriate conditions. These results compare well with experiment even in many details, proving in turn the relevance of the model.

Table of Contents

1. Introduction

The thermal stability of a radiating tokamak edge plasma against radial perturbations has been considered in various papers, e.g. [1–3]. Poloidal variations were usually excluded because of the high classical electron heat conduction, $\kappa_{\|}$, along field lines, enforcing nearly constant temperature on magnetic flux surfaces. On the other hand, because of the $T^{5/2}$-dependence of $\kappa_{\|}$, substantial gradients along field lines are to be expected at typical tokamak (or stellarator) edge temperatures ($\lesssim 100\,\mathrm{eV}$), if there are sufficiently strong, localized energy sinks caused, for instance, by hydrogen recycling or impurity radiation. Such localized perturbations may be imposed externally or they may develop spontaneously as the result of a thermal instability starting from an initially much more homogeneous equilibrium.

For the principal mechanism, it is not important, whether the corresponding field lines form closed flux surfaces or intersect material walls. In the latter case, the wall (e.g. a limiter or target plate) acts as a specific local sink of energy and charged particles and a source of neutrals. A well-documented example of this type is the high-recycling divertor, where most of the heating power is dumped and strong temperature gradients along field lines in the scrape-off layer are needed to drive the required heat flux. Even in this case, the spontaneous formation of the cool, high recycling region above a certain edge density may be regarded as the result of an instability, the onset of which is, however, clearly related to the location and design of the divertor, which can be changed at will.

Self-enhanced impurity radiation cooling, on the other hand, seems to be the dominant cooling mechanism driving the spontaneous formation of the "marfes" discovered some time ago, e.g. [4–7] and observed now in almost any tokamak. Under ideal circumstances (e.g. in the "predisruptive state" of ASDEX ohmic double-null divertor discharges [5]) the marfe shows up as an axisymmetric, cold and strongly radiating belt layer at the high-field side of the torus, located radially at or just inside the magnetic separatrix. This global structure and its reproducibility seem to contradict the adopted hypothesis of thermal instability caused by insufficient heat conduction along field lines. But the remaining sensitivity of the poloidal position against weak perturbations (e.g. a very small vertical shift of the plasma column in ASDEX) despite the inherent poloidal asymmetry imposed by toroidal curvature support the basic idea, as will be shown.

In addition to the two examples discussed above, there could be a variety of edge phenomena, which are also related to the thermal stability problem, but have attracted little attention so far in experiment. The reason for the latter could be that most of

the instabilities and asymmetries to be expected would *not* have such a simple, global structure like a "marfe". Because of the low cross-field transport within magnetic flux surfaces, instabilities could be confined to narrow magnetic flux bundles, forming helical perturbations with finite wavelength along field lines not necessarily corresponding to one poloidal revolution as in a normal marfe. In terms of the standard tokamak notation these instabilities, based on the same physical mechanism as the marfe, would correspond to fairly high toroidal and poloidal wave numbers. They could be responsible for part of the low frequency, high amplitude edge fluctuations observed in tokamaks around the separatrix. Because of the same basic mechanism, they should occur under similar conditions as marfes and even in connection with them, especially for "radiating edge" conditions (cold plasma mantle, photosphere), which may be considered as the end product of a poloidally expanding marfe. Such instabilities could also be triggered externally, e.g. by local hydrogen and impurity gas puffing (or recycling at local structures), by laser-driven impurity blow-off or by pellet injection. Because of their narrow helical structure, they would be invisible for most diagnostics and, if not discovered and corrected for, they could cause severe misinterpretation of results. Probably there is also a class of more complex hybrid modes in the edge region involving also other sources of free energy. These modes are, however, beyond the scope of this report.

In the present paper we try to quantify at least part of the speculations pointed out above. For this purpose, we first derive analytically the dispersion relation of a homogeneous, radiating edge plasma for two-dimensional perturbations and give stability criteria for strong and moderate collisionality, using non-equilibrium radiation cooling rates. In the second part, we present extensive numerical simulations, which are basically one-dimensional along field lines, but also include several crude approximations of cross-field transport. These calculations rely on an appropriately modified code package originally built for simulations of the ASDEX divertor scrape-off layer. The model includes all the relevant hydrogen and impurity dynamics along field lines, non-equilibrium radiation cooling and a non-local electron heat flux formulation. Finally, the results are discussed and compared with experiments. A few specific points are treated in more detail in the appendix.

Clearly, it would be desirable to have a fully two-dimensional code for the edge region like those under development in several laboratories. These are, however, not yet sufficiently advanced, especially with respect to impurities which play the crucial role in the present context.

2. Linear Stability Analysis of a Homogeneous, Radiating Plasma

The interpretation of a marfe as the result of a thermal instability along field lines was already discussed in refs. [4, 5] and crude stability estimates were given. These considerations are extended in this section by deriving the general dispersion relation of two-dimensional periodic perturbations in a homogeneous, collisional and radiating plasma embedded in a constant magnetic field. The main purpose is to assess the basic mechanisms and to derive stability criteria and scaling laws as a basis for the numerical calculations described below, and for comparison with existing experiments and extrapolation to future ones.

We start from fluid equations along field lines for the hydrogen plasma (spatial coordinate s) allowing in addition for perpendicular heat conduction

$$\begin{aligned} \frac{\partial n}{\partial t} + \frac{\partial}{\partial s}(n v_\parallel) &= 0 \\ \rho \frac{\partial v_\parallel}{\partial t} + \rho v_\parallel \frac{\partial v_\parallel}{\partial s} + \frac{\partial p}{\partial s} &= 0 \\ \frac{3}{2}\left[\frac{\partial p}{\partial t} + \frac{\partial}{\partial s}(p v_\parallel)\right] + p\frac{\partial v_\parallel}{\partial s} + \frac{\partial}{\partial s} q_\parallel + \frac{\partial}{\partial x} q_\perp &= P_H - P_{\mathrm{RAD}} \end{aligned} \tag{1}$$

Here n is the electron or ion density, $v_\parallel$ the parallel velocity, $\rho = n m_H$ the hydrogen mass density (m_H = hydrogen mass), $p = 2nT$ is the total pressure assuming equal ion and electron temperatures ($T_i = T_e = T$; T is taken in energy units throughout this paper).

The perpendicular heat flux $q_\perp = -\kappa_\perp \nabla_\perp T$ will be taken anomalous according to the usual tokamak experience. For the parallel heat flux $q_\parallel$ one would normally take the Spitzer-Härm form, $q_{\parallel \mathrm{SH}} = -\kappa_\parallel \nabla_\parallel T$ with $\kappa_\parallel \sim T^{5/2}$. But since the mean free path of the extreme tail electrons carrying the heat flux is frequently comparable or even larger than the parallel wavelengths $\lambda_\parallel$ to be considered, we include a non-local form of the parallel heat flux proposed by Luciani et al. [8] which extends the validity of our model into a less collisional regime ($\lambda_0 \ll \lambda_\parallel$, but $\lambda_{\mathrm{HC}} \sim O(\lambda_\parallel)$, where λ_0 and $\lambda_{\mathrm{HC}} \approx 45\lambda_0$ are the mean free paths of bulk ($\overline{E}_e = T/2$) and "heat conduction tail electrons", resp.[8]). In the limit of small periodic perturbations to be considered, this model simply leads to a correction factor for the classical Spitzer-Härm heat flux q_{SH} of the form

$$q_\parallel = q_{\mathrm{SH}}/(h_\parallel^2 \lambda_{\mathrm{HC}}^2 + 1), \quad h_\parallel = 2\pi/\lambda_\parallel \tag{2}$$

The effective heat flux $q_\parallel$ obviously increases $\sim T^{7/2}$ for $h_\parallel \lambda_{\mathrm{HC}} \ll 1$, but decreases $\sim T^{-1/2}$ for $h_\parallel \lambda_{\mathrm{HC}} \gg 1$ because of $\lambda_0 \sim T^2/n$.

For a homogeneous equilibrium, the equations (1) reduce to $P_H = P_{\mathrm{RAD}}$, where P_H is an external heating power (simulating also the divergence of the perpendicular heat flux in a real boundary layer) and $P_{\mathrm{RAD}} = n n_I L_I(T)$ is the power radiated away by impurities of density $n_I \ll n$ according to their specific cooling rate $L_I(T)$.

We linearize eqs. (1) around the equilibrium values of density and temperature, n_0 and T_0, by choosing

$$T = T_0[1 + \eta \cos(h_\parallel s) \cos(h_\perp x) \exp(\gamma t)]$$

and

$$n = n_0[1 - \epsilon \cos(h_\parallel s) \cos(h_\perp x) \exp(\gamma t)].$$

$h_\parallel$ and $h_\perp$ are the parallel and perpendicular wavenumbers of the perturbation, γ the damping or growth rate, and ϵ, $\eta \ll 1$ are the expansion parameters. P_{RAD} is approximated in the vicinity of n_0, T_0 by $P_{\mathrm{RAD}} \sim n^\mu T^\nu$. $\mu = 1$ means that n_I is constant and independent of the perturbation (e.g. no friction between hydrogen and impurities), while $\mu = 2$ means that hydrogen and impurities move together (strong coupling). With these assumptions we obtain the following dispersion relation*

$$\begin{aligned} &\gamma^{*3} + \gamma^{*2}\left[(\omega_0 \tau_{\mathrm{HC}})^{-1} + \nu(\omega_0 \tau_{\mathrm{RAD}})^{-1}\right] \\ &+ \frac{5}{3}\gamma^* + (\omega_0 \tau_{\mathrm{HC}})^{-1} - (\mu - \nu)(\omega_0 \tau_{\mathrm{RAD}})^{-1} = 0 \end{aligned} \tag{3}$$

Here $\gamma^* = \gamma/\omega_0$, $\omega_0^2 = 2T_0 h_\parallel^2/m$ is the isothermal sound frequency, τ_{RAD} and τ_{HC} are the characteristic radiation cooling and heat conduction times, respectively, defined by $\tau_{\mathrm{RAD}} = 3n_0T_0/P_{\mathrm{RAD}}$ and $\tau_{\mathrm{HC}} = (\tau_{HC\parallel}^{-1} + \tau_{HC\perp}^{-1})^{-1}$ with the perpendicular heat conduction time

$$\tau_{HC\perp} = 3n_0T_0/(\kappa_\perp T_0 h_\perp^2) = 3/(\chi_\perp h_\perp^2)$$

and the parallel one

$$\tau_{HC\parallel} = 3n_0T_0(1 + h_\parallel^2 \lambda_{\mathrm{HC}}^2)/(\kappa_\parallel T_0 h_\parallel^2) = 3(1 + h_\parallel^2 \lambda_{\mathrm{HC}}^2)/(\chi_\parallel h_\parallel^2)$$

where $\kappa = n\chi$ has been used. It is in τ_{HC} where the long mean free path correction finally appears (this point has been unprecisely formulated in an earlier conference abstract [10]).

Eq. (3) has three roots (at least one real), which are shown in Fig. 1 for specific cases. Fig. 1a assumes no radiation and therefore the sound wave dispersion at finite heat conduction ($\gamma_{2,3}$) is obtained in addition to a purely damped branch (γ_1). A more

* An equivalent relation was independently derived by T. Stringer. [9]

detailed discussion of the sound waves is deferred to Appendix I. In Fig. 1b the radiation is continuously increased at fixed, normalized heat conduction and $\mu = 2$, $\nu = 0$. Apart from the modification of the sound waves, the real branch becomes unstable ($\gamma_1 > 1$) above a critical, normalized radiation power. Fig. 1c shows at fixed radiation power and heat conduction the dependence on the radiation exponent $\nu = \partial(lnP_{\mathrm{RAD}})/\partial(lnT)$. An unstable branch is obtained for $\nu < \nu_{crit}$, where ν_{crit} is even positive ($\nu_{crit} \leq \mu$ as a consequence of $p \approx$ const. near the marginal point, causing $P_{\mathrm{RAD}} \sim n^{\mu}T^{\nu} \sim T^{\nu-\mu}$). This is in contrast to the case $h_{\|} = 0$, where $\nu_{crit} \lesssim 0$ and which is *not* contained in eq. (3) (see Appendix II)

Typical growth rates close to the marginal point are $\gamma \ll \omega_0$, but increase rapidly to $\gamma \gtrsim \omega_0$ far beyond. As an example we get $\omega_0 \approx 1.3 \times 10^4\,\mathrm{s}^{-1}$ for $\lambda_{\|} = 30\,\mathrm{m}$ (as appropriate for a marfe), $T = 20\,\mathrm{eV}$, $n \approx 10^{19}\,\mathrm{m}^{-3}$, yielding e-folding times of a fraction of a millisecond. The corresponding eigenfunctions are determined by $\eta = \epsilon(\gamma^2/\omega_0^2 + 1)$ together with the ansatz for the perturbation, the relative pressure variation along field lines being of order $\gamma^2/{\omega_0}^2$. A convenient approximation of (3) for γ, τ_{HC}^{-1}, $\tau_{\mathrm{RAD}}^{-1} \ll \omega_0$ is $\gamma \approx (\mu - \nu)/\tau_{\mathrm{RAD}} - 1/\tau_{\mathrm{HC}}$, while for $\tau_{\mathrm{RAD}}^{-1} \gg \tau_{\mathrm{HC}}^{-1}, \omega_0$ we get $\gamma \sim -\nu/\tau_{\mathrm{RAD}}$.

From the dispersion relation (3) a quite simple criterion for *in*stability is obtained,

$$(\mu - \nu)\tau_{\mathrm{HC}} > \tau_{\mathrm{RAD}}, \tag{4}$$

and $\nu < \mu$ clearly is a necessary criterion. For $(\mu - \nu) \sim O(1)$ and positive, i.e. a destabilizing radiation characteristic, instability requires that the local radiation cooling acts faster than the heat conduction opposing it, a result expected tentatively. The criterion (4) might be cast in various forms, depending on what is kept fixed, e.g. a criterion for a critical value of $\nu, n_0, n_I, T_0, h_{\|}, h_{\perp}, \chi_{\perp}$ or combinations of them. Here we just give, as an example of practical interest, the scaling of the critical impurity concentration, $C = n_I/n$, for two regimes of collisionality and $\tau_{HC\perp} \gg \tau_{HC\|}$.

For $h_{\|}^2\lambda_{\mathrm{HC}}^2 \ll 1$,

$$C_{crit} \approx 1.8 \times 10^3 T^{7/2} h_{\|}^2/[(\mu - \nu)n^2 L(T)] \tag{5a}$$

is obtained (T in eV, otherwise standard units; a Coulomb logarithm $ln\Lambda = 13.6$ corresponding to 100 eV, $10^{20}\,\mathrm{m}^{-3}$ is arbitrarily used). Instability ($C > C_{crit}$) for a given impurity is obtained most easily at low temperature, long wavelength and high density, a regime applying typically to the marfing edge in ALCATOR, FT, etc..

For $h_{\|}^2\lambda_{\mathrm{HC}}^2 \gg 1$ together with $\lambda_{\mathrm{HC}} \approx 7.5 \times 10^{16} T^2/n$ the critical concentration becomes a function of temperature only, independent of n and $h_{\|}$:

$$C_{crit} \approx 3 \times 10^{-31}/[(\mu - \nu)\sqrt{T}L(T)] \tag{5b}$$

(units as in (5a)). This regime would apply to marfe-type perturbations at low edge density and high temperature but also to correspondingly shorter wavelengths at higher collisionality, i.e. whenever $\lambda_{\|} < 7.5 \times 10^{16} T^2/n$. These perturbations would appear in experiment probably as local fluctuations rather than global modes like the marfe.

In order to get numbers we have numerically calculated non-equilibrium radiation cooling rates $L(T)$ for various impurity species, using atomic data sets of K.H. Behringer [11]. Figure 2 shows the results assuming a stationary source of singly charged impurities and a finite impurity residence time τ_I, the physically relevant number being the product $n\tau_I = 10^{16}\,\mathrm{sm}^{-3}$ (further details are given in Appendix III). This is the only point in our model where we implicitly take account of the impurity cross-field transport, which was neglected in eqs. (1) for simplicity. But while the latter causes only a minor error and could be qualitatively accounted for by a factor of less than two reduction of $\tau_{HC\perp}$, $L(T)$ can change by an order of magnitude when τ_I changes (see Appendix III).

Assuming now, for example, carbon impurities, $T = 10\,\mathrm{eV}$, $n = 3 \times 10^{19}\,\mathrm{m}^{-3}$, $\lambda_{\|} = 30\,\mathrm{m}$ ($h_{\|}^2 \lambda_{\mathrm{HC}}^2 \ll 1$), and $\mu = 2$, eq. (5a) yields $C_{crit} \approx 0.1\%$. On the other hand, taking chromium, $T = 100\,\mathrm{eV}$, $n = 3 \times 10^{18}\,\mathrm{m}^{-3}$, $\lambda_{\|} \ll 250\,\mathrm{m}$, (i.e. $h_{\|}^2 \lambda_{\mathrm{HC}}^2 \gg 1$) and $\mu - \nu \approx 2$, then eq. (5b) applies and $C_{crit} \approx 5\%$ is obtained, corresponding to an absolute chromium density of $1.5 \times 10^{17}\,\mathrm{m}^{-3}$. It is obviously more difficult to drive instabilities in this less collisional regime, but our model also becomes less reliable there, as discussed later on.

Finally, we mention that instead of impurities the cooling can be caused also by hydrogen neutral radiation and ionization, in which case the cooling rate and the mass source are coupled. A specific example is the divertor recycling, where in addition to the hydrogen radiation cooling self-trapping of neutrals enhances the instability. These processes are extensively discussed in the literature (see review [12]) and therefore omitted here.

A further straight-forward extension of the present analysis is the inclusion of a temperature-dependent local heating, e.g. ohmic heating or absorption of externally launched particles or waves. Clearly, apart from the different sign, a temperature-dependent power input acts in the same way as radiation losses: In eq.(1) it is the total temperature variation of $(P_H - P_{\mathrm{RAD}})$ which determines stability.

3. Numerical Simulations

3.1 Model and Numerical Codes

Numerical solutions of the fully nonlinear, one-dimensional hydrogen and impurity dynamics along field lines were obtained from a modified version of the hydrodynamic code SOLID [13] coupled with a multi-fluid impurity code [14, 15] *. In the latter, each impurity charge state is treated as a test fluid which is coupled to neighbouring states by ionization and recombination and to the hydrogen majority by collisions (friction and thermal forces) and the electric field. A finite impurity life time simulating cross-field losses is included and the impurity sources can be chosen arbitrarily. The non-equilibrium radiation cooling (including ionization energy) is calculated from the actual charge state distribution using again data compiled by K.H. Behringer [11]. In SOLID the non-local heat conduction model of ref. [8] has been implemented [16] and in both codes, the boundary conditions have been generalized, such that application to the scrape-off layer as well as to closed flux surfaces is possible (left: reflecting symmetry, right: reflecting symmetry or absorbing target plate). The length of the computational volume will be denoted by L. In this paper, only results for closed field lines are presented.

The impurity code takes $n, T_e, T_i, v_{||}$ and the parallel electric field $E_{||}$ from SOLID, solves the coupled charge state equations and calculates the radiation cooling power, which is then fed back into the electron energy balance of SOLID as an additional loss term (to be added in ref. [13]). In addition, there is a feedback loop acting on the electron power input of SOLID (h_e in ref. [13]), which can be used to control the average pressure or temperature on the considered flux tube or local power influx in proportion to the local perpendicular temperature difference with respect to isothermal neighbouring flux surfaces, etc.. Such a feedback loop allows to model various edge scenarios including qualitatively the thermal coupling with neighbouring flux surfaces, which otherwise would require a fully two-dimensional model not yet available. Finally, one should remember that the test fluid assumption for the impurities requires $\sum_z n_z Z^2 \ll n$, where n_z is the density of Z times charged impurities, i.e. Z_{eff} at the edge should be close to one for the model to be quantitatively correct. This condition is reasonably satisfied for a typical average impurity charge state $\bar{Z} \lesssim 4$ at the edge (Fig. 2) for concentrations up to a few percent.

---

* There is a printing error in the momentum equation of ref.[14]: The sign of the term $\partial V_Z^2/(2\partial s)$ should be positive; compare ref.[15]

3.2 Non-linear Instabilities in an Initially Homogeneous Plasma

For comparison with the analytic model and for identification of new mechanisms introduced by the more sophisticated numerical model, we first investigate initially homogenous plasmas. As a typical example we take carbon as impurity in a plasma with $T = 10\,\mathrm{eV}$, $n = 3 \times 10^{19}\,\mathrm{m}^{-3}$, and an impurity residence time $\tau_\perp = 3\,\mathrm{ms}$ in the edge layer. We assume a steady homogeneous source of singly charged carbon ions and $L = 15\,\mathrm{m}$, simulating a connection length $l_{con} \sim \pi q R$ between low- and high-field side, i.e. a marfe-type perturbation (R is the major torus radius, q the safety factor). For this case the analytic model predicted a marginal carbon content of $n_c \sim 3 \times 10^{16}\,\mathrm{m}^{-3}$, while in the simulation a weak instability becomes visible first at around $6 \times 10^{16}\,\mathrm{m}^{-3}$. With $7.5 \times 10^{16}\,\mathrm{m}^{-3}$ the growth time is already in the millisecond range and a nonlinear saturation is obtained at a perturbation of about 10%. Apart from inaccuracies in the analytical model, the higher critical concentration obtained numerically may be caused by incomplete coupling of carbon with hydrogen, especially because of the thermal diffusion of impurity ions towards high temperature and therefore opposite to the hydrogen mass motion. Its influence should be strong as long as the expected growth rates are comparable to the typical thermal diffusion time.

In Fig. 3 the results for $n_c = 1.5 \times 10^{17}\,\mathrm{m}^{-3}$ are presented which clearly reveal the most significant features of a nonlinear thermal instability. The most important quantities are shown for $s = 0$ and $s = 15\,\mathrm{m}$ (i.e. 180° apart in phase). Starting from a weakly perturbed carbon concentration $n_c \sim (1 - 0.001 \cos \pi s/L)$ an instability develops with $\gamma \approx 1.5 \times 10^3\,\mathrm{s}^{-1}$. After 5 ms the maximum amplitude is obtained with a density and temperature asymmetry factor of ~ 6.5 (Fig. 3ab). The pressure perturbation is only a few percent as expected from the analytical model ($\sim \gamma^2/\omega_0^2$). The asymmetry of the carbon distribution (Fig. 3c) is weaker (~ 3.6) than that of hydrogen and reaches its maximum somewhat earlier. In the subsequent, roughly stationary and moderately asymmetric state, the impurity asymmetry even reverses sign. Again the reason is that carbon does not move strictly together with hydrogen but lags behind because of inertia and the retarding thermal force [14, 15]. The latter becomes even dominant when the hydrogen motion slows down, while the thermal diffusion proportional to $Z^2 \partial \mathrm{T}/\partial \mathrm{s}$ still continues to drive carbon ions towards the high temperature side. A stationary state is nevertheless possible because of the finite impurity residence time $\tau_\perp$ together with an external carbon source, replacing the carbon ions, wherever they are lost, by a spatially homogeneous distribution.

In contrast to the carbon density the radiation loss (Fig. 3d) remains appreciably higher at the cool high density side, where at $t = 12\,\mathrm{ms}$ $CIII$ (i.e. $Z = 2$) dominates, while at

the high- temperature side about 70% of the carbon is CV, which does not radiate at that temperature. The *average* cooling rate decreases during the instability because of the complicated redistribution of impurities in space and over charge states. A global thermal runaway (i.e. a $h_{||} \equiv 0$ instability as discussed in Appendix II) is nevertheless avoided by controlling the spatially homogeneous energy input in such a way that the *average* temperature is kept about constant.

For $\tau_\perp = \infty$, the impurity accumulation would stop only when

$$\partial(lnp_I)/\partial s \approx \bar{Z}^2 \partial(lnT)/\partial s,$$

where $p_I = n_I T$ is the impurity pressure. Long before, however, radiation cooling at the hot side rises to a level, where an instability occurs, but now in the opposite direction, and so on. In this way, relaxation oscillations are obtained as shown in Fig. 4, with 0.25% of oxygen in a hydrogen plasma of $n = 10^{20}\,\mathrm{cm}^{-3}$, $T = 15\,\mathrm{eV}$ and $\tau_\perp \to \infty$, i.e. an extreme and somewhat unphysical case, but similar results are frequently obtained for $\tau_\perp$ down to the millisecond range.

The occurence of nonlinear relaxation oscillations and their amplitude and frequency depend on a few more details, like the shape of $L(T)$ in a larger vicinity of the equilibrium temperature and how far it is away from the marginal temperature, where $(\mu - \nu) \approx 0$. It also depends on the ratio of the actual impurity concentration to the marginal one. For carbon such relaxations are easily obtained for the example in Fig. 3, if the temperature is lowered to $5 - 8\,\mathrm{eV}$.

A quite instructive overview of the possible effects is presented in Fig. 5, showing a density rise scenario at constant plasma pressure of $3 \times 10^{20}\,\mathrm{eV\,m^{-3}}$ and a constant *average* carbon density of $3 \times 10^{17}\,\mathrm{m}^{-3}$($\tau_\perp = 3\,\mathrm{ms}, C^{1+}$ source $= 10^{20}\,\mathrm{m}^{-3}\,\mathrm{s}^{-1}$). Starting at $n = 10^{19}\,\mathrm{m}^{-3}$ and $T = 30\,\mathrm{eV}$, the plasma is stable. With increasing density and decreasing temperature a thermal instability similar to that in Fig. 3 occurs at $T_e \approx T_i \approx 14\,\mathrm{eV}$, the phase being predetermined here by a very weak asymmetry of the carbon source of only one percent. A marfe-type, highly asymmetric equilibrium is formed. The critical temperature for onset is only weakly dependent on the impurity density n_I and the wavelength $\lambda_{||}$ as expected from eq. (5a), which yields $T_{\mathrm{crit}} \sim n^{2/9}/h_{||}^{4/9}$ for $nT = \mathrm{const.}$, if we neglect the temperature dependence of $(\mu - \nu)L(T)$ in that range. Below $8\,\mathrm{eV}$ the stationary asymmetry is destroyed and subsonic relaxation oscillations occur as discussed above. Their frequency increases from 60 Hz to nearly 200 Hz in this specific case before they disappear below $4\,\mathrm{eV}$ and a homogeneous, stable equilibrium is reached again in accordance with $(\mu - \nu) < 0$ in this range.

A qualitatively similar behaviour is obtained for other low-Z impurities and the analytical scaling relations obviously provide a reasonably accurate guide line. A material of specific interest for future machines is beryllium. It is different from neighbouring elements because of the continuously increasing radiation with decreasing temperature ($\nu < 0$ for $T \lesssim 10\,\mathrm{eV}$). Numerically rather fast instabilities with large nonlinear amplitude are obtained in the eV-range even at quite low concentrations as predicted analytically. Stabilization of these Be-driven modes is only possible via perpendicular transport ($\tau_{HC\perp}$ in eq.(4)), since parallel heat conduction becomes rather inefficient in the eV-range and ν is destabilizing.

The oxygen radiation maximum is shifted by a factor of about 2.5 towards higher temperature compared to that of carbon (Fig. 2). Therefore a similar behaviour as for carbon would be expected at correspondingly higher temperature and impurity concentration ($T^{7/2}$), provided everything else is kept roughly constant. In fact, relaxation oscillations are readily obtained for $T \lesssim 15\,\mathrm{eV}$, a typical case showing 250 Hz for $n \approx 1.5 \times 10^{19}\,\mathrm{m}^{-3}$, $n_O = 2 \times 10^{18}\,\mathrm{m}^{-3}$, $T \approx 15\,\mathrm{eV}$, $\lambda_\parallel = 2L = 30\,\mathrm{m}$ and $\tau_\perp = 3\,\mathrm{ms}$ (compare also Fig. 4). For this case, $h_\parallel \lambda_{HC\parallel} \approx 0.24$ holds and the classical heat conduction formula still appplies. With further increased temperature (at fixed n and $h_\parallel$) the long mean free path corrections become important and the $T^{7/2}$-dependence is no longer valid as discussed earlier.

In view of large experiments with connection lengths $l_{con} \approx 50\,\mathrm{m}$ and higher edge temperature for marfing conditions, the following density rise scenario with oxygen impurities may be instructive: $L = 100\,\mathrm{m}$, $n_O = 5 \times 10^{17}\,\mathrm{m}^{-3}$; $p = 5 \times 10^{20}\,\mathrm{eV\,m}^{-3}$; starting values $n = 10^{19}\,\mathrm{m}^{-3}$; $T = 50\,\mathrm{eV}$. Figure 6 shows the time variation of n and T at $s = 0$ and $s = 100\,\mathrm{m}$, or at the torus outside and inside, if interpreted as a marfe perturbation with $L = l_{con}$. Starting at $T \lesssim 40\,\mathrm{eV}$ an asymmetric state is formed, initiated by a fast instability, causing some numerical difficulty (a non-equidistant grid is used in this run in order to handle the extreme density peak at $s = 100\,\mathrm{m}$ and $t \approx 8.5\,\mathrm{ms}$).This state changes slowly during density rise until at an average density $\bar{n} \geq 5 \times 10^{19}\,\mathrm{m}^{-3}$ it collapses and starts to oscillate. The quiescent phase in between is characterized by a continuous change of the spatial profiles as shown in Fig. 7. Clearly, the cold and dense plasma expands along field lines at the expense of the hot region. Figure 8 shows the charge state distribution along field lines and the corresponding radiation cooling for $t = 35\,\mathrm{ms}$. Apart from a small peak caused by local hydrogen mass flow into the marfe and a backward thermal force, the total impurity density is nearly constant along field lines because of the homogeneous source and the small $\tau_\perp$. There is, however, a pronounced structure of individual charge states and hence of their radiation along field lines according to the temperature variation especially of the

ionization rates. As a consequence, the total cooling rate has a maximum just in the transition region, where intermediate charge states radiate. Part of this loss is covered by heat conduction from the hot end, where the local radiation cooling is quite low, mainly because of the very small radiation of helium-like $O\ VII$. In the marfe, parallel heat conduction is negligible and the temperature adjusts such that the cooling rate just balances the instantaneous heating rate assumed to be homogeneous in this case. The long mean fee path correction is not yet dramatic, though $h_{\|}\lambda_{HC\|} \sim O(1)$ at the hot end. The maximum temperature there decreases only by about 10% if the classical, local heat flux model is used.

Runs have been made with various charge states and mixtures for the impurity source. Two tendencies turned out to be important: Highly ionized source particles ($\geq O\ VII$, e.g. from the hot plasma core) contribute very little to radiation, and recombination to lower, radiating charge states is usually not significant since recombination times are at best comparable to $\tau_{\perp}$. The global thermal behaviour therefore does not change very much if such high-Z source particles are simply ignored. The result mainly depends on the total input of radiating charge states. On the other hand, the actual charge state distribution and hence the spectroscopically observed line radiation depends remarkably on the source mixture. For instance, the OII-radiation increases rapidly during marfe formation in any case, but the absolute intensity can be an order of magnitude lower if there are no OII-particles in the local source. Only when the impurity life time in the marfe is tens of milliseconds, then the charge state distribution approaches equilibrium and becomes independent of the source.

It is important to note that in the previous example (Figs. 6-8) $\sum n_z Z^2 \ll n_e$ holds in the marfe, but $\sum n_z Z^2 \approx n_e$ at the hot end and therefore the test particle assumption becomes marginal. An estimate of the expected error in various terms (e.g. inertia, electron mean free path and heat conduction, thermal force) suggests that the global behaviour should still be qualitatively correct. A quantitative description would require a much more ambitious model anyway, and the present one is already rather complex.

Simulations were made also in the $h_{\|}^2\lambda_{HC\|}^2 \gg 1$ regime. Assuming $T_e \gtrsim 150\,\mathrm{eV}$, $n_e \lesssim 5 \times 10^{12}\,\mathrm{m}^{-3}$ and chromium as impurity, marfes were obtained only for a chromium concentration of 5 to 10 percent as expected from linear theory. In this regime, however, not only the test particle assumption is questionable but also the fluid model, despite the non-local heat flux model. Therefore the result should be taken as indicative only.

3.3 Results for Inhomogeneous Power and Impurity Input

A nonlinear thermal stability analysis of a tokamak or stellarator edge layer for arbitrary modes inherently requires a three-dimensional code not yet existing. It is only for axisymmetric modes in an axisymmetric tokamak (poloidal divertor or toroidal limiter) that a strictly two-dimensional treatment is sufficient (e.g. marfes). Since our present code is basically one-dimensional (along a constant magnetic field), we cannot hope to get quantitatively correct results even for the axisymmetric case. Nevertheless, a quite reasonable qualitative information is obtained by an appropriate choice and control of local energy and particle sources and sinks representing the poloidally varying cross-field transport in a real geometry.

Let us assume a narrow radiating edge layer with radial width w and temperature T surrounding a hot, thermally stable core with temperature $\hat{T}$ just inside the unstable layer. The temperature outside the radiating zone may be zero. The local radial energy input into the radiating layer is then given for n, $\chi_\perp \approx$ const. across the layer by $\mathrm{div} q_\perp \approx n\chi_\perp(\hat{T} - 2T)h_\perp^2$, with $h_\perp \approx w^{-1}$. Starting at the torus outside (poloidal angle $\theta = 0$) and following a helical magnetic flux bundle, $\chi_\perp$ may vary along field lines as well as the width w, the latter being proportional to the local ratio of toroidal to poloidal magnetic field (Fig. 9).

In our code this coupling to a neighbouring isothermal layer at varying perpendicular distance is approximated by a local power input $P_H \sim (\bar{T} - T)f(s)$ or alternatively $P_H \sim (\bar{p} - p)g(s)$, where $\bar{T}$ and $\bar{p}$ are prescribed average values and $f(s), g(s)$ represent the poloidal variation of the cross-field transport as discussed above. It is interesting to note that $P_H \sim (\bar{T} - T)$ is stabilizing for all modes (equivalent to finite $\tau_{HC\perp}$ in the analytic theory), while $P_H \sim (\bar{p} - p)$ according to a pressure-gradient-driven perpendicular transport does not affect slow $h_\parallel \neq 0$-modes but still prevents thermal run-away of the layer ($h_\parallel = 0$-mode), as already demonstrated for homogeneous equilibria.

The radial impurity transport is more complex since locally radial drifts (caused by the parallel force balance) may be more important than the usual anomalous diffusion, and also because of ionization and recombination. In the code this problem is simplified by the same procedure as with a homogeneous plasma: An impurity source with a prescribed charge state mixture and spatial distribution along field lines balances the particle loss represented by a single, constant residence time $\tau_\perp$ for all charge states. Because of the lack of a reasonably simple model for impurity cross-field transport, experimental results may be taken as a guideline for the impurity source distribution.

In the first example pressure feedback is used and $g(s) \sim exp(-(2s/L)^2)$, according

to a rather strong poloidal asymmetry of radial transport, if $s = 0$ is identified with $\theta = 0$ and $s = L$ with $\theta = 180°$ (inside). In between, s and θ are not necessarily proportional, since the pitch angle of the field line may vary. We need not specify in this approximation whether $\chi_\perp$ or w or both change poloidally. Similar to Fig. 5, a density rise scenario with carbon impurities ($n_c = 2.4 \times 10^{17}\,\mathrm{m}^{-3}$) has been simulated. Apart from the slower density rise chosen, the major difference to the homogeneous power input is that the fast initial phase and the large relaxation oscillations disappear and the marfe-type perturbation expands slowly and smoothly in poloidal direction until a weakly asymmetric cold layer is formed. Figure 10 shows a sequence of spatial temperature and density profiles demonstrating again the "poloidal" growth of the marfe (compare Fig. 7).

The sensitivity against a power input asymmetry has been checked by using $g(s) \sim (1 + \alpha \cos \pi s/L)$ and varying α. Runs were also made with homogeneous power input ($g(s) = \text{const.}$), but an asymmetric impurity source $\sim (1 - \beta \cos \pi s/L)$. In both cases the relaxation oscillations again appeared for α, $\beta \lesssim 0.5$ in the form of a moderate oscillation of the marfe size, converging to the large relaxation oscillations of Fig. 5 for α,$\beta \lesssim 0.2$. Obviously a substantial asymmetry of the input power or the impurity concentration is needed to get a stationary marfe.

In all these asymmetric input cases the marfe formed where it was expected: At the point where the power input was lowest or the impurity concentration highest. On the other hand, starting from a true equilibrium, any phase or sign of the linear perturbation should be possible as in the homogeneous case, except that the eigenfunctions are not as simple. The answer is that in the calculations and probably also in experiment we never start from a true, quiescent equilibrium and, in addition, the nonlinear terms *are* dependent on the phase and sign of the perturbation, favouring certain modes, the selection being the stronger, the larger the asymmetry of the equilibrium. Starting from some initial state, the nonlinear calculation runs into a final stable state according to an appropriately defined energy minimum (not necessarily an absolute one). Alternatively a quasi-stationary, fluctuating state may be reached, since we are dealing with an open system with high energy throughput.

From the examples above the results for more complex distributions may be qualitatively inferred. If there is, for instance, in a tokamak an in-out asymmetry of radial transport, and in addition an up-down asymmetry of the impurity concentration, then a marfe is to be expected somewhere above or below the midplane depending on the sign and magnitude of both perturbations.

Another case of practical interest is an elliptical plasma with magnetic separatrix not far behind the front of a limiter or a poloidal divertor geometry. As can be seen in Fig. 9, the width w of the edge layer is largest at top and bottom for this case and there is an in-out asymmetry of w which increases with plasma pressure. The principal effect is shown by taking the same hydrogen and impurity density scenario as in Fig. 6, but with inhomogeneous power input $P_H(s) = 5\times10^5(T(s)/\bar{T}-1)(1+\alpha_1\cos\pi s/L+\alpha_2\cos 2\pi s/L)$, where α_1 describes the in-out asymmetry and α_2 the widening at top and bottom, and $\bar{T} = 80\,\mathrm{eV}$ is taken. In addition to the explicit spatial asymmetry introduced by α_1 and α_2, an implicit spatial variation of the power input dependent on the local electron temperature has been included as a further step towards a realistic description. The absolute numbers chosen correspond to an effective perpendicular heat conduction time of $\tau_{HC\perp} \approx 0.5\,\mathrm{ms}$ about equal to $\tau_{HC\parallel}$ at $n = 10^{19}\,\mathrm{m}^{-3}$, $T = 35\,\mathrm{eV}$. Therefore, perpendicular and parallel transport have a comparable effect on the thermal instability in this case in contrast to the examples described before, where the average pressure was feedback-controlled equivalent to $\tau_{HC\perp} \gg \tau_{HC\parallel}$. Taking somewhat arbitrarily $\alpha_1 = 0.2$ and $\alpha_2 = 0.8$, a marfe is clearly formed half way between outside and inside, i.e. somewhere at top and bottom, as expected. Figure 11 shows the evolution of the electron temperature profile in time. Lines of constant T_e are given in a (s,t)-plane for an interval of 32 ms, during which the average electron density rises from $10^{19}\,\mathrm{m}^{-3}$ to $3\times10^{19}\,\mathrm{m}^{-3}$. In this phase, a weak in-out oscillation of the top (or bottom) marfe shows up with a tendency to coalescence at inside. Lowering α_2 and increasing α_1, the marfe switches over to inside, since longer wavelengths are less stabilized. The tendency to relaxation oscillations for α_1, $\alpha_2 \ll 1$, as obtained earlier at constant average plasma pressure, is recovered with the present more realistic model. As a counterpart to the top-bottom marfe, Fig. 12 shows the result for $\alpha_1 = 0.3$ and $\alpha_2 = 0$, everything else being unchanged. Though the marfe formation at inside and the poloidal growth towards a homogeneous cold plasma mantle during the density rise is in accord with earlier results, the behaviour is rather complex in detail. Even more complicated graphs are obtained if the density or radiation of individual charge states is monitored, a fact which can cause great difficulties when interpreting spectroscopic measurements from a marfing tokamak edge. In this context codes like the present one may be helpful.

The last problem to be considered is that of local marfes initiated by localized sources. In principle, the calculation proceeds in the same way as above, since also the basic mechanism is the same. The main difference is that the impurity source is now confined to a narrow region and frequently, but not necessarily, to a short time interval. For convenience any explicit variation of the perpendicular transport along field lines is neglected ($f(s)$=const.). It is assumed that a flux Φ_c of carbon hits the plasma surface

and is ionized in a narrow layer to produce a volume source Q_c of $C\ II$. The source region may have a width of the order of one meter along field lines; the poloidal width does not directly enter, but determines for a given safety factor q the effective field line length to be considered, i.e. the topology of the helical flux bundle on which the local marfe is created. For a poloidal extent of $\sim 120°$ and $q \approx 3$ the length between the source region and some symmetry point should be $L \approx 3\pi R$.

We choose arbitrarily $L = 50\,\mathrm{m}$, $n = 10^{19}\,\mathrm{m}^{-3}$, $\bar{T} = 15\,\mathrm{eV}$ and local temperature feedback according to a perpendicular heat conduction time $\tau_{HC\perp} \approx 2\,\mathrm{ms}$. A peaked $Q_c(s)$ with a decay length of about 2m along field lines and a maximum of $10^{20}\,\mathrm{m}^{-3}\,\mathrm{s}^{-1}$ is taken. Together with a perpendicular particle loss time of $\tau_\perp = 3\,\mathrm{ms}$ a local impurity density maximum of $n_c \approx 3\times10^{17}\,\mathrm{m}^{-3}$ is obtained, if the source duration is long enough, e.g. 10 ms for the present example. During the initial impurity rise a local marfe forms with a temperature below 3 eV. At the far end the temperature only drops by about 10%, since the perpendicular power influx prevents cooling of the total helical flux tube. In Fig. 13 a contour plot of the $C\ III$ density in a (s,t)-plane is presented (top). Lines of constant temperature are given also (bottom).

For lower source strength the marfe reduces to a weak perturbation, while a higher influx of impurities causes an earlier and faster local marfe formation. A smaller spatial source width requires a higher source strength, since obviously the total number of impurities is the relevant quantity. There is a natural widening of the radiating region because of parallel classical impurity diffusion and thermal forces. For typical edge conditions this spreading of low charge states is also of the order of one meter. The analytic stability criteria of a homogeneous plasma are not directly applicable, but can be used as a guide line if an *average* impurity concentration on the flux bundle is used instead of the local maximum.

There is also a global consideration which might illustrate the danger of local cool spots or cool helical flux bundles to occur: assume that there is a *homogeneous* impurity density in a tokamak such that the edge is close to global marfing conditions. If this impurity content is maintained by a source which is *localized* (where the localization along field lines is less important, as discussed), then the radiation is strongly enhanced on the involved flux bundle, and the stability condition should be already strongly violated there. A further enhancement occurs if the same impurity content is established transiently by an impurity source pulse short compared to the global confinement time. Therefore it seems to be difficult in a real tokamak to have significant average impurity content without having strong local density and temperature asymmetries in the edge around the sources.

4. Discussion and Comparison with Experiment

It has been concluded already in earlier papers [4, 5, 9, 10] that impurity radiation in conjunction with insufficient parallel electron heat conduction should be the basic mechanism responsible for the poloidally asymmetric, toroidally symmetric "marfes" observed in the tokamak edge region. This conclusion is confirmed by our detailed analytical and numerical study. In fact, the examples given have been chosen to represent typical marfing edge conditions and a rather convincing similarity between numerical results and experiment is evident, e.g. the conditions for formation and poloidal growth of the marfe towards a homogeneous cold plasma mantle. The fact that the marfe preferentially starts at the high-field side can be explained by a poloidally asymmetric radial transport, for which there is clear experimental evidence in ASDEX (derived from power flow to inner and outer divertor plates with double null divertor).

A power flow asymmetry of more than a factor of two is also needed in the numerical simulation to reduce or suppress the subsonic relaxation oscillations, which seem to be absent in most tokamaks (or have not yet been detected). It is only in the Frascati Tokamak (FT) that strong oscillations of up to 100% modulation are sometimes observed (Fig. 5 of ref. [6]). The striking similarity with the relaxation oscillations discovered in our calculations may be an indication for the relevance of our parallel impurity flow model including thermal forces which play a key role in this context.

On the other hand, the perpendicular impurity transport, described by a finite residence time $\tau_\perp$, is the weakest point in our model, since locally radial drifts may be important and can cause a complicated two-dimensional flow pattern. In experiment impurity density asymmetries of the order of a factor two are frequently observed. If included in the simulation, such an asymmetry has a clear influence on the marfe position and relaxation similar to that of the power flow asymmetry. It may partly explain why a marfe is formed not exactly at the inside and why its position is sometimes slowly varying. With respect to up-down marfes in elliptical plasmas or poloidal divertor experiments, there is not yet sufficient experimental material available for comparison.

A common experimental finding is that there is a critical line-integrated density $\bar{n}$ for marfe formation roughly proportional to the toroidal current or to q^{-1} [4, 5, 7, 17], sometimes coinciding with the global density limit. At first glance this seems to contradict the stability criterion in eq. (5a), which is much more complicated. In experiment, however, there is a continuous radial temperature profile and for fixed $h_\parallel$ and n, C_{crit} has a minimum at a temperature slightly above the value where $(\mu - \nu)$ becomes negative. Inserting this temperature and rewriting eq. (5a) as a criterion for a

critical edge density we obtain

$$n_{\mathrm{crit}} \sim h_{\|} C^{-0.5} \sim q^{-1} C^{-0.5}$$

The required dependence is therefore obtained if the impurity concentration C and the profile shape (i.e. $\bar{n}/n$) do not significantly change with current or if the two weak effects tend to cancel. The inverse dependence of the critical density on the impurity concentration has been observed also [4]. The scaling should be the same for a marfe occurring in the scrape-off layer or on closed flux surfaces. Depending on the actual geometry, however, the absolute numbers could be different.

The two-dimensional shape of a stationary marfe in the poloidal plane should be roughly lense-type, since on the hottest unstable flux surface the marfe should just start near the midplane, while closer to the cool high-field side edge the poloidal extent increases. The lowest charge states should radiate in the cold centre of the marfe, while according to the simulation, the radiation is highest in the transition region to the hot plasma, where intermediate charge states contribute. This theoretical picture agrees with photographs taken at ASDEX in the light of various spectral lines [5]. It is also consistent with various line-integrated horizontal measurements. The sensitivity of the marfe position to a vertical shift of the plasma in ASDEX is obviously a consequence of the temperature decay along the separatrix towards the active divertor chamber, forcing the marfe in the same direction.

In experiment, various impurities may contribute simultaneously. The most likely candidates in present experiments are low-Z ions like carbon and oxygen, as shown in the preceding sections. The metal content is usually too low to be significant. A material of specific interest for future applications is beryllium. Because of its destabilizing radiation characteristic in the eV-range, it may drive thermal instabilities in the cold scrape-off layer wing. In fact, because of the high Be content to be expected with Be limiters and the high specific cooling rate for non-equilibrium edge conditions (Fig. 2), the total radiation could be substantial in that region. Experimental results relevant to this problem are just coming up.

Our analytical and numerical studies suggest that, in addition to the global axisymmetric marfe, more localized three-dimensional modes should occur. They could be restricted to individual helical magnetic flux bundles because of low radial and poloidal cross-field transport and their parallel wave number $h_{\|}$ would be determined by the stability criterion. Modes with smaller $h_{\|}$ than the standard marfe should be unstable at lower impurity concentration, and could appear as precursors. Shorter wavelength modes could be unstable somewhere also when a global marfe is present. In experiment such

modes are more difficult to detect. Probably they would arise in the form of high amplitude density and temperature fluctuations at the edge. The subsonic relaxation oscillations around 100 Hz have been already discussed above. It is not clear, however, whether edge fluctuations at higher frequency ($\gtrsim 1\,\mathrm{kHz}$) are related to thermal stability also. Experimentally a correlation between marfes and edge fluctuations is sometimes observed. Probably, there is some transition region to the usual magneto-hydrodynamic modes, but these are beyond the scope of the present paper.

A final question of high relevance to experiment is that of local impurity sources. As discussed at the end of the preceding chapter, it is quite likely that a local marfe is created during localized impurity puffing or laser blow-off. Depending on absolute numbers the cool region may extend helically along and across field lines. Like the standard marfe, such a perturbation may readily trigger disruptions as frequently observed or simply suppress the power flow into the divertor, as observed in ASDEX for certain parameters [18]. Another inherent localized impurity source is the limiter. A stationary, self-limiting marfe encompassing the limiter and a residual flux of hot ions providing the sputtering source could be considered in cases where the thermal load onto the limiter seems to be anomalously low. In any case, such poloidal and toroidal asymmetries may be the key point with respect to the "missing energy" problem in nearly every tokamak.

5. Conclusions

Analytical and numerical investigations of the thermal stability of a collisional radiating plasma relevant to the edge of magnetic confinement fusion experiments were presented. Fluid equations were used with long mean free path corrections for the electron heat flux and a realistic non-equilibrium radiation model has been included.

The general dispersion relation for two-dimensional perturbations in a homogeneous, radiating plasma was derived, yielding modified sound waves and an aperiodic branch, which can be unstable. Stability criteria for short and long mean free paths of heat conduction electrons were given. The basic mechanism for thermal instability, i.e. radiation cooling together with insufficient thermal conduction, was confirmed.

Numerical calculations were performed including all the relevant dynamics of hydrogen and impurities along field lines and their collisional (thermal force and friction) and electrostatic coupling. Cross field transport of energy and impurities was simulated quite realistically by appropriately controlled local sources and sinks. These calculations yield a quite detailed picture of global and local marfe formation, its growth along field lines

or, equivalently, in poloidal direction, and the possible transition to a stable radiating edge. Relaxation oscillations have been discovered in a wide range of parameters and the distribution of individual impurity charge states and their radiation pattern turns out to be rather complex. Density rise scenarios, elliptical plasmas, fluctuations and localized cool spots near impurity sources were simulated for typical impurities between Be and Cr by appropriately choosing the space- and time-dependent input parameters and the field line length.

Comparing with experiments, a surprising similarity between numerical results and various measurements was stated. Apart from the global marfe history, this is true also for such details as the relaxation oscillations observed in the Frascati tokamak. This agreement supports the confidence that the physical model chosen provides, in fact, a realistic description of the thermal stability problem of the edge region and justifies extrapolation to future experiments.

Acknowledgements

We thank Dr. K.H. Behringer (JET/IPP) for providing his impurity data sets and subroutines and for continuous advice for their application.

Appendix I. Sound Waves at Finite Heat Conduction

Neglecting radiation, eq. (3) describes the dispersion of sound waves at finite heat conduction (Fig. 1a). The modes are weakly damped because of electron heat transport, the maximum damping rate being about 15% of the real frequency ω at $\omega\tau_{HC} = 1$ in agreement with the result of A.R. Bell, Phys. Fluids **26**, 279 (1983).

It is interesting, however, to note that including the non-local heat flux model in the linearized form of eq. (2) the isothermal limit cannot be reached with hydrogen ions. In fact, the *maximum* normalized heat conduction rate for hydrogen ions ($Z = 1$) is

$$(\omega_0\tau_{HC\|})^{-1} \approx 0.35\sqrt{A},$$

where A is the atomic weight of the hydrogen isotope. This maximum occurs at $h_\|\lambda_{HC\|} = 1$. Therefore sound waves in a hydrogen plasma are usually adiabatic or at best in the transition region and the right part of Fig. 1a is not accessible in contrast to the case of an ideal Lorentz gas.

Appendix II. Stability of $h_\| = 0$ Modes

Because of the plasma dynamics along field lines inherent in $h_\| \neq 0$ modes, there is no smooth transition to $h_\| = 0$ and therefore this simpler case must be treated separately. For $h_\| = 0$, $h_\perp \neq 0$ we get

$$\gamma^* = -\nu(\omega_0\tau_{RAD})^{-1} - (\omega_0\tau_{HC,\perp})^{-1}.$$

The instability criterion for the trivial case $h_\| = h_\perp = 0$ is $\nu < 0$ independent of the impurity content. The more practical case $h_\perp \neq 0$, equivalent to a *radial* perturbation in an unstable edge layer of finite thickness $\Delta \sim h_\perp^{-1}$, yields instability for $\nu < -\tau_{RAD}/\tau_{HC,\perp}$. (A more complicated dispersion relation for purely radial modes including also finite impurity transport was derived by Lengyel and Goedheer (Report IPP 1/191; Garching (1981)) and applied to numerically calculated radiating edge profiles.)

Comparing with the criterion for $h_\| \neq 0$ modes it is clear that for $\mu > \nu > -\tau_{RAD}/\tau_{HC\perp}$ only poloidally asymmetric modes can be unstable. Therefore, poloidally asymmetric modes like marfes will usually appear *before* a radiating edge can be set up.

Appendix III. Non-Equilibrium Radiation Cooling Rates

The ionization and recombination rates and the radiation cooling from individual charge states needed in our numerical simulations are calculated by implementing into our 1D code package data sets and subroutines kindly provided by K. H.Behringer [11].

A simplified 0D version of the code package has been used to calculate the non-equilibrium radiation cooling rates for a homogeneous plasma and finite impurity residence time, as needed for the analytical stability estimates. Graphs for various impurities were presented in Fig. 2 of the main paper. A few more details are given here.

Fig. III-1 shows for oxygen the dependence of the cooling rates on $n\tau_I$. There is little change at the low temperature side but a strong influence above the first maximum. The result for carbon is qualitatively similar, while for beryllium the cooling rate decreases also at low temperature when $n\tau_I$ increases.

Figure III-2 shows for oxygen the influence of the charge state of the source particles replacing the lost ones. There is only a moderate dependence below the helium-like state as expected. The latter and higher states contribute very little to radiation and recombination to lower charge states is still a small effect. If, however, sufficient hydrogen neutrals are present, then charge exchange recombination into radiating states causes again a strong increase of the cooling rate.

There is a severe lack of data for metals in the desired temperature range and results should be used with caution. In fact, the graph for iron shown in [10] was calculated from an earlier, incomplete data set and should be dropped.

References

[1] N. Ohyabu, Nucl. Fusion **19** (1979), 1491.

[2] J. Neuhauser, *Characteristics of a Radiating Layer near the Boundary of a Contaminated Plasma*, IPP Report 1/182, Max-Planck-Institut für Plasmaphysik, Garching (1980).

[3] D.E.T.F. Ashby, M.H. Hughes, Nucl. Fusion **21** (1981), 911.

[4] B. Lipschultz, B. LaBombard, E.S. Marmar, M.M. Pickerell, J.L. Terry, et al., Nucl. Fusion **24** (1984), 977.

[5] H. Niedermeyer, K.H. Behringer, K. Bernhardi, A. Eberhagen, G. Fussmann, et al., *Change of Plasma Properties Prior to High Density Disruptions in ASDEX*, IPP Report III/80, Max-Planck-Institut für Plasmaphysik, Garching (1983), and 11th European Conference on Controlled Fusion and Plasma Physics, Aachen, 1983, Europhysics Conference Abstracts **7D-I** (1983), 43–46.

[6] F. Alladio, R. Bartiromo, B. Casali, P. Buratti, F. Demarco, et al., Phys.Lett. **A90** (1982), 405.

[7] D.R. Baker, R.T. Snider, M. Nagami, Nucl. Fusion **22** (1982), 807.

[8] J.F. Luciani, P. Mora, J. Virmont, Phys. Rev. Lett. **51** (1983), 1664.

[9] T.E. Stringer, *A Theory of Marfes*, , 12th European Conference on Controlled Fusion and Plasma Physics, Budapest, 1985, Europhysics Conference Abstracts **9F-I** (1985), 86–89.

[10] J. Neuhauser, W. Schneider, R. Wunderlich, ibid **9F-II** (1985), 476–79.

[11] K.H. Behringer, P.G. Carolan, B. Denne, G. Decker, W. Engelhardt, et al., *Impurity and Radiation Studies During the JET Ohmic Heating Phase*, Report JET-P(85)08, JET Joint Undertaking, Abingdon, UK (1985); submitted for publication; (see also [14], sect. 4).

[12] K. Lackner, M. Keilhacker, J. Nucl. Mater. **128&129** (1094), 368.

[13] W. Schneider, D.B. Heifetz. K. Lackner, J. Neuhauser, D.E. Post, K.G. Rauh, J. Nucl. Mater. **121** (1984), 178.

[14] J. Neuhauser, W. Schneider, R. Wunderlich, K. Lackner, K.H. Behringer, J. Nucl. Mater. **121** (1984), 194.

[15] J. Neuhauser, W. Schneider, R. Wunderlich, K. Lackner, Nucl. Fusion **24** (1984), 39.

[16] K. Lackner, U. Ditte, G. Fussmann, T. Grave, G. Janeschitz, et al., Plasma Physics and Contr. Nucl. Fusion Research 1984, (Proc. 10th Int. Conf. London 1984), Vol. 1, 319, IAEA Vienna (1985).

[17] J. O'Rourke, D. Campbell, B. Denne, A. Gondhalekar, N. Gottardi, et al., *Poloidally Asymmetric Edge Phenomena in JET*, 11th European Conference on Controlled Fusion and Plasma Physics, Budapest 1985, Europhysics Conference Abstracts **9F-I** (1985), 155–158.

[18] G. Fussmann, W. Poschenrieder, K. Bernhardi, B. Richter, Z. Szymanski, et al., J. Nucl. Mater. **121** (1984), 164.

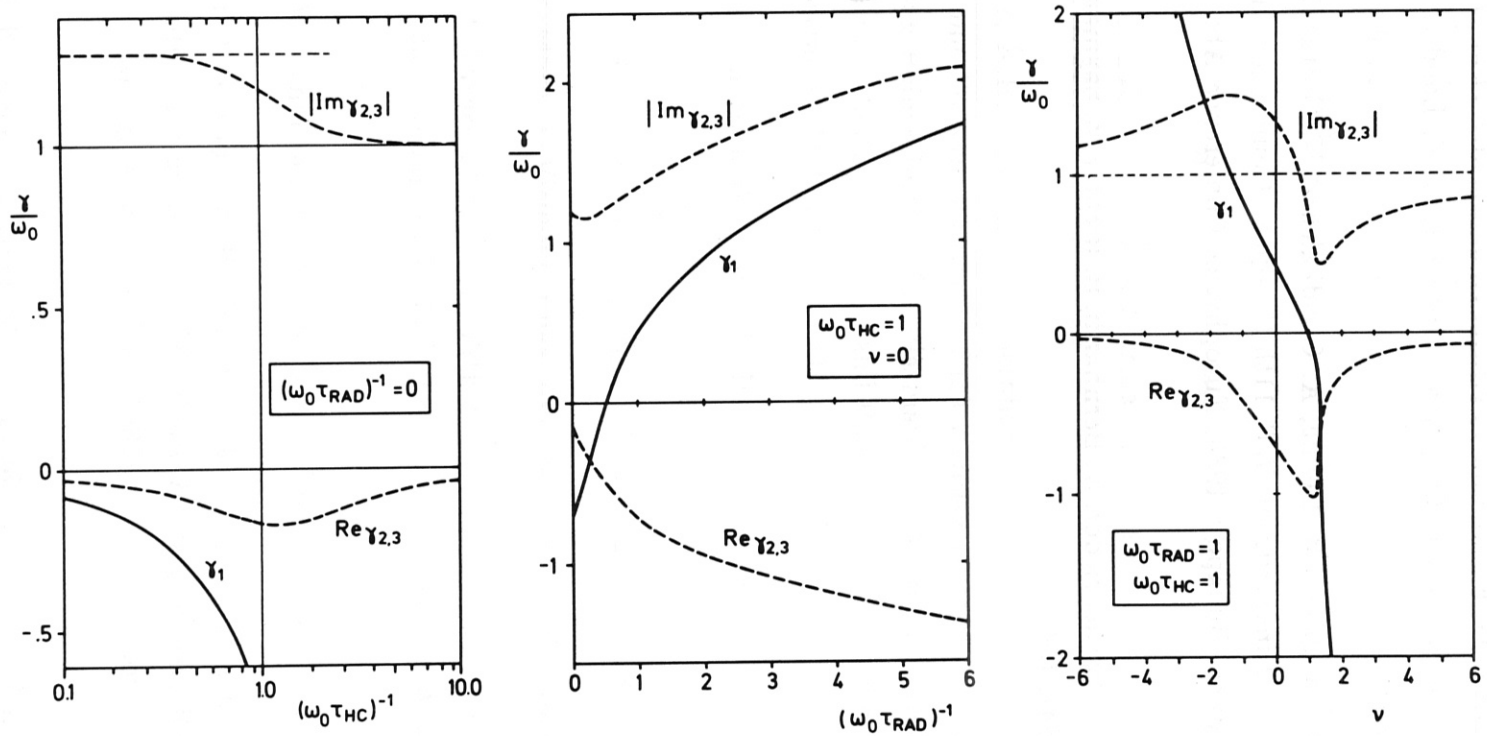

Fig. 1 Dispersion diagrams of a homogeneous plasma in a longitudinal magnetic field. The roots of eq. (3) are shown as function of the normalized heat conduction time (a), the normalized radiation cooling time (b) and the radiation exponent ν (c).

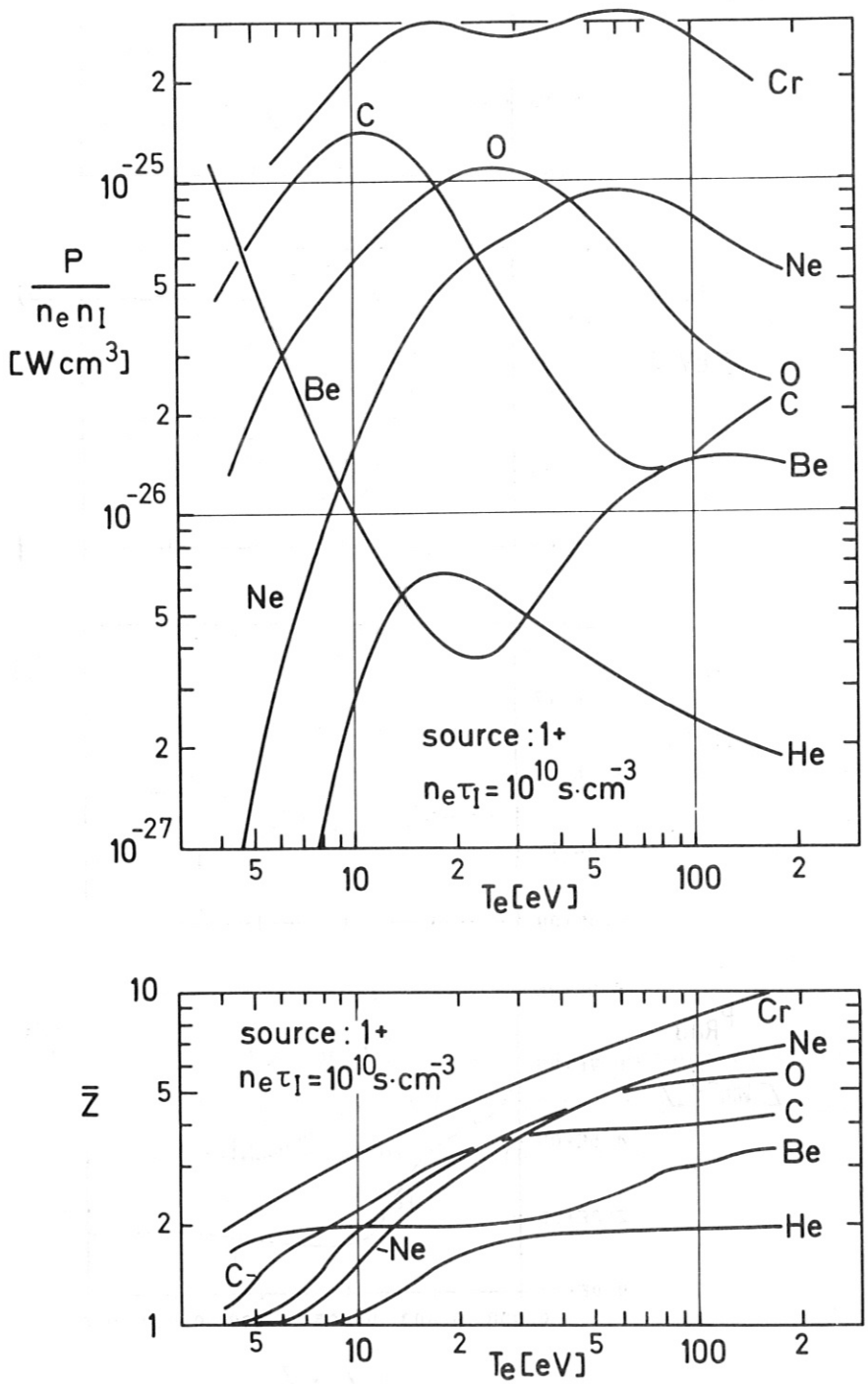

Fig. 2 Non-equilibirum radiation cooling rates and average charge states $\bar{Z}$ for various impurities and finite impurity residence time as function of electron temperature (numerically calculated from data of K. Behringer [11]). A continuous source of singly charged impurities is assumed.

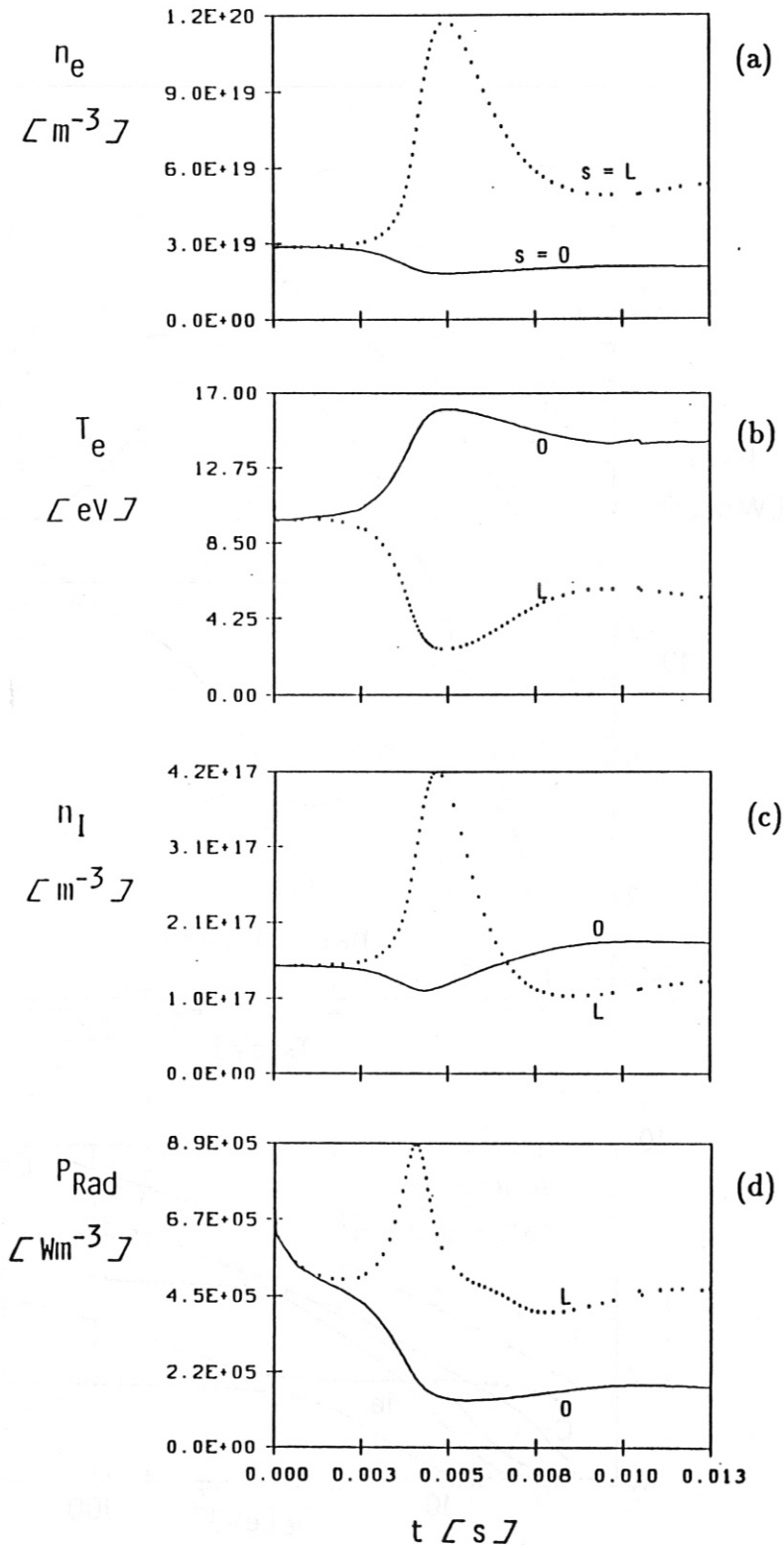

Fig. 3 Nonlinear evolution of a thermal instability along field lines at constant average pressure ($\tau_{HC\perp} \to \infty$). The electron density (a) and temperature (b), the total impurity density (c) and radiation cooling power (d) are shown as monitored at both ends of the computational volume, i.e. half a wavelength of the initial perturbation apart (carbon impurities, $\tau_\perp = 3\,\mathrm{ms}$, initial perturbation $\lambda_\parallel = 2L = 30\,\mathrm{m}$).

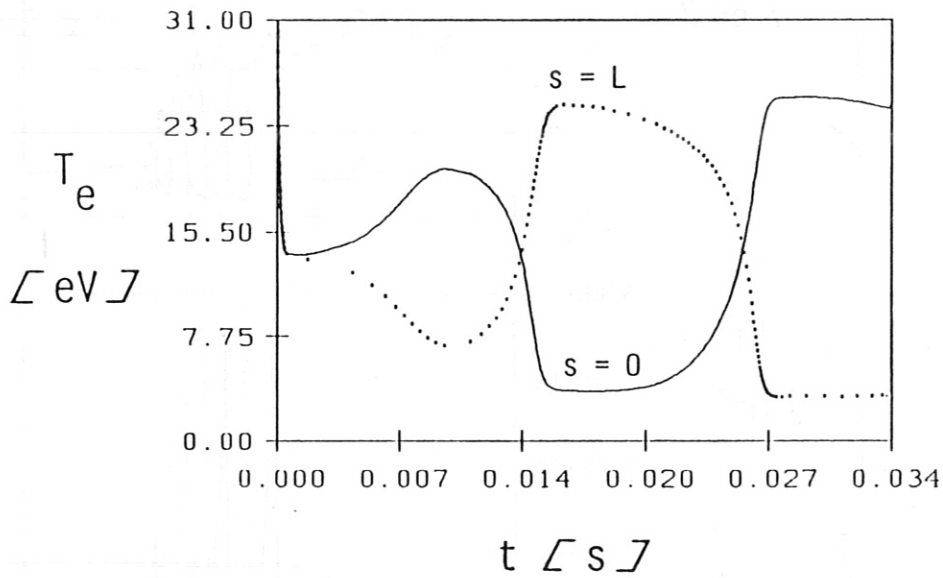

Fig.4 Nonlinear thermal relaxation oscillations caused by decoupling of hydrogen and impurities (e.g. thermal forces). Only the electron temperature is shown at the two ends of the computational volume (average densities: $n = 10^{20}\,\mathrm{m}^{-3}$, $n_0 = 2.5 \times 10^{17}\,\mathrm{m}^{-3}$, $L = 15\,\mathrm{m}$, $\tau_\perp = 3\,\mathrm{ms}$).

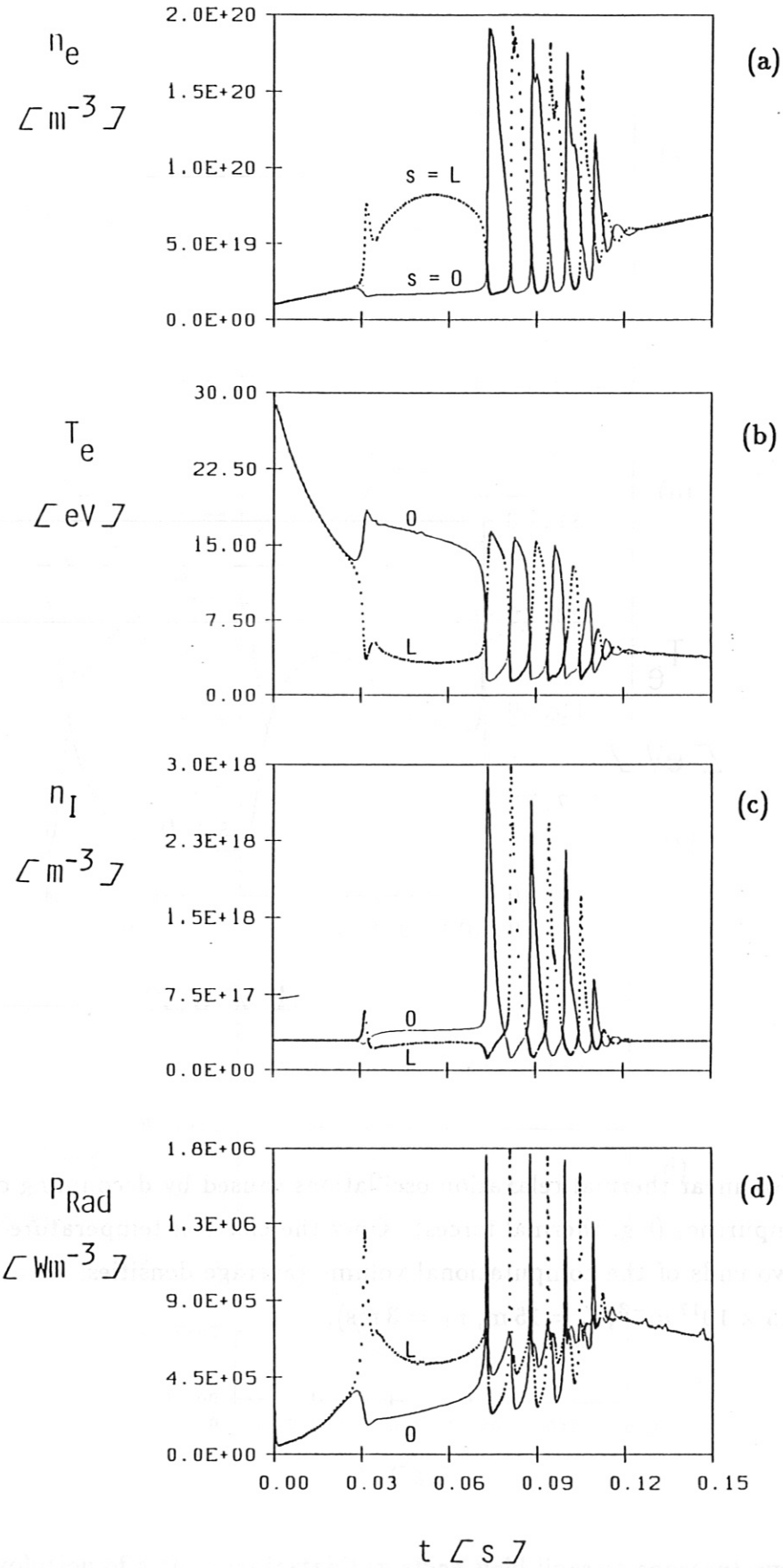

Fig. 5 Nonlinear thermal instability and relaxation oscillations during a continuous plasma density rise at constant average plasma pressure and carbon impurity content. As in Fig. 3, the values of electron density (a) and temperature (b), the impurity density (c) and radiation cooling (d) are presented at opposite ends ($\tau_\perp = 3\,\mathrm{ms}; L = 15\,\mathrm{m}$).

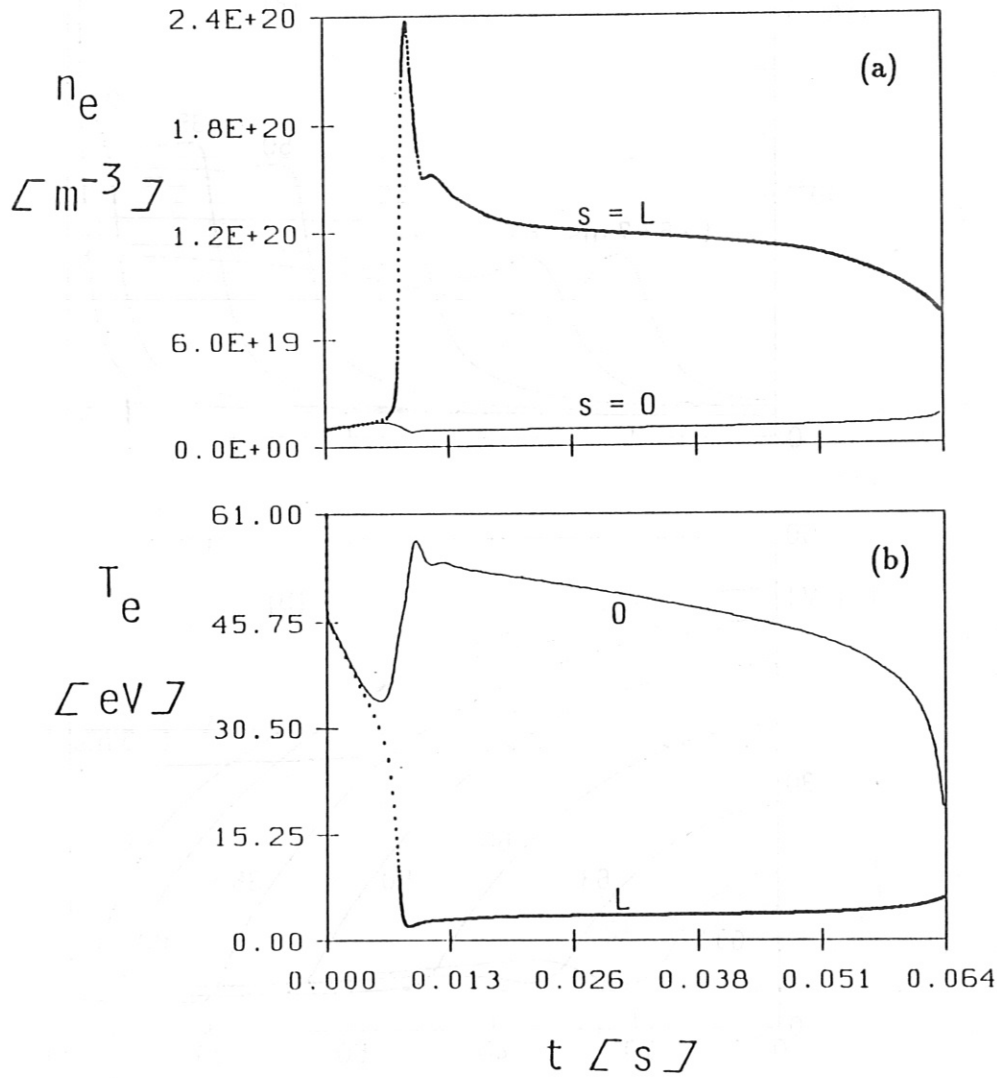

Fig. 6 Nonlinear thermal instability during a continuous plasma density rise at constant average plasma pressure and oxygen impurity content. Electron density (a) and temperature (b) are shown at opposite phases ($\bar{n}_O = 5 \times 10^{17}\,\mathrm{m}^{-3}$, $\tau_\perp = 3\,\mathrm{ms}$, $L = 100\,\mathrm{m}$). In contrast to Fig. 5, the instability starts at substantially higher temperature as expected.

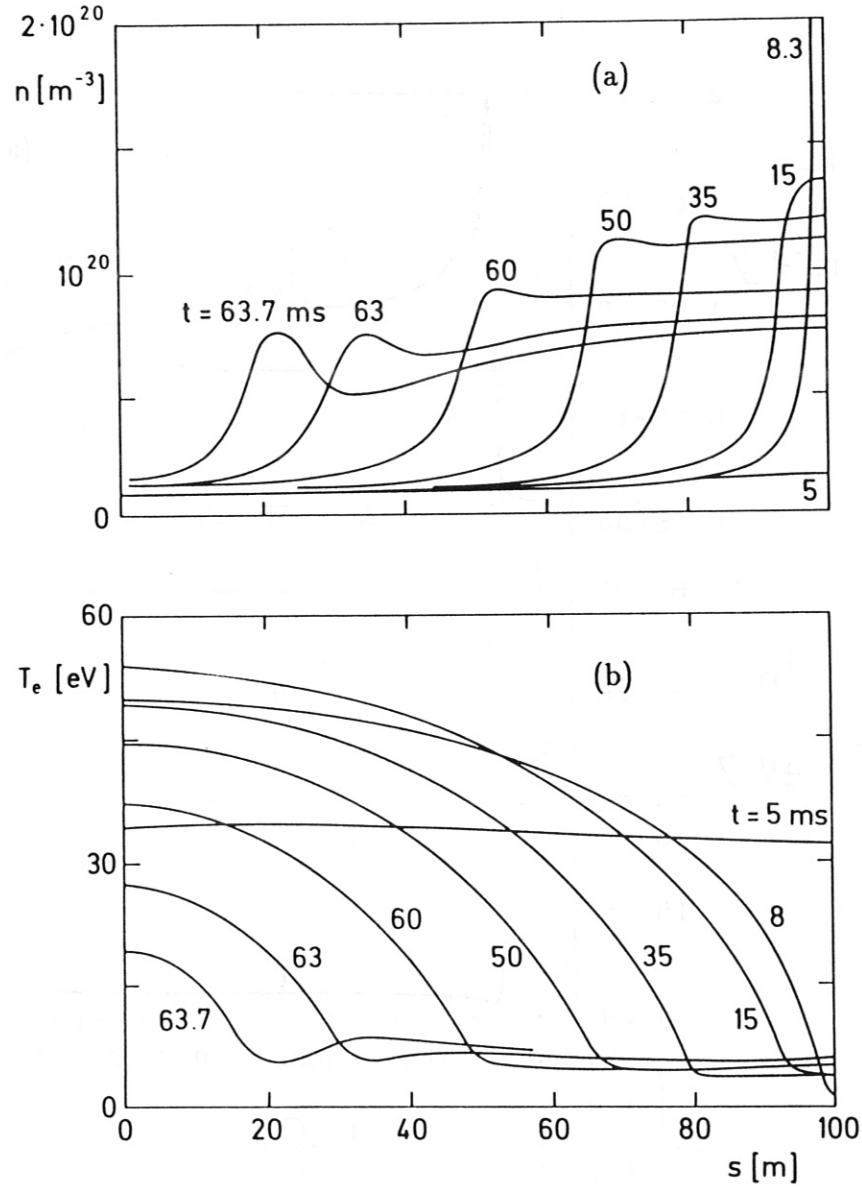

Fig. 7 Sequence of spatial electron density (a) and temperature (b) profiles along field lines for the case of Fig. 6, demonstrating the continuous expansion of the cool region (marfe) with increasing electron density.

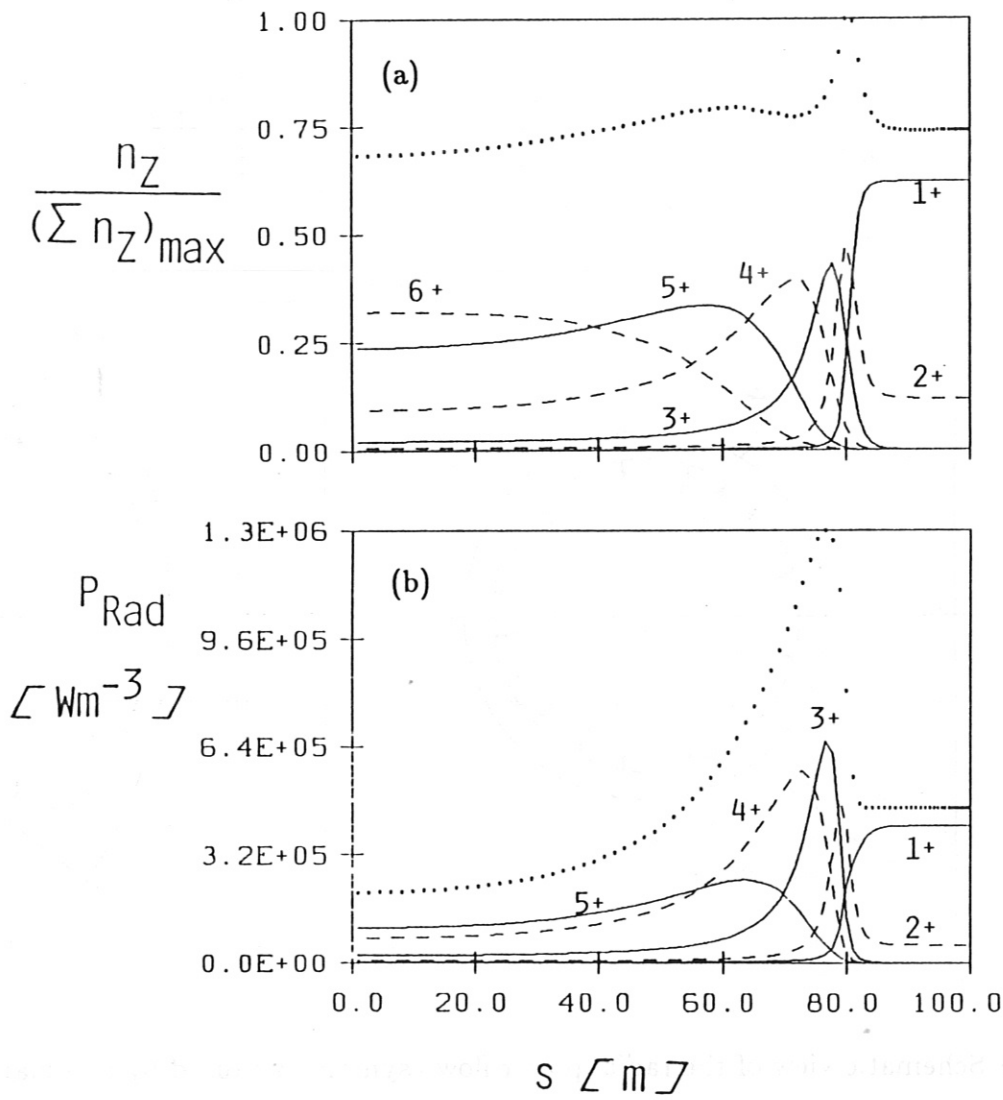

Fig. 8 Density distribution (a) and radiation (b) of individual charge states along field lines for the same case as in Figs. 6 and 7 at $t = 35$ ms. The dotted lines represent the sum over all charge states.

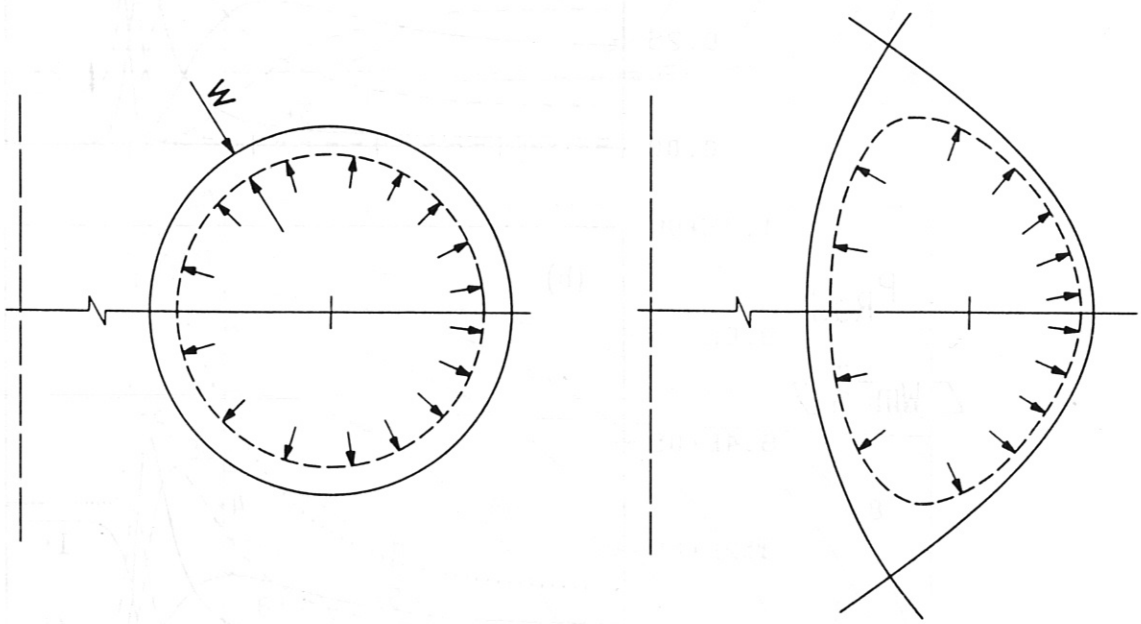

Fig. 9 Schematic view of the radial power flow asymmetry caused by poloidal variation of $\kappa_\perp$ and w in a circular or an elliptical, separatrix bounded plasma.

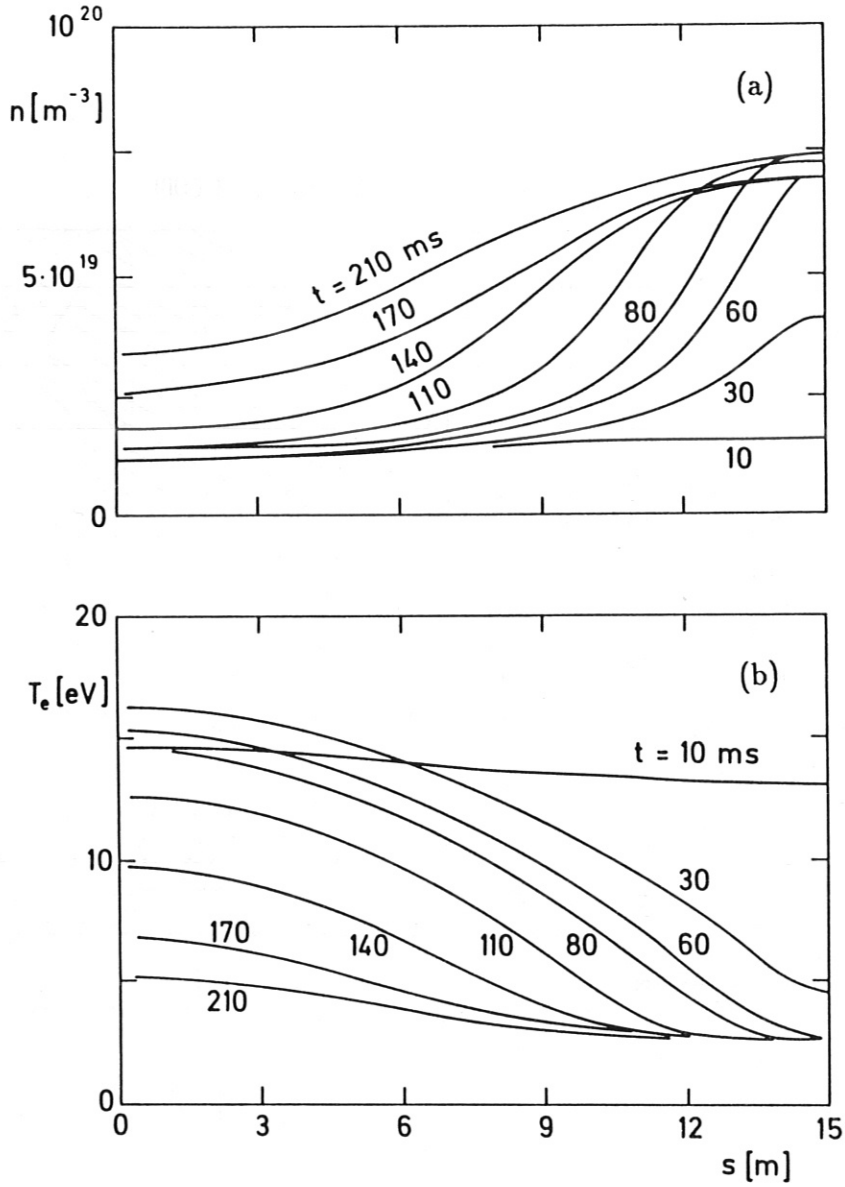

Fig. 10 Sequence of spatial electron density (a) and temperature (b) profiles along field lines for a similar scenario as in Fig. 5 (density rise at constant average pressure), but with highly asymmetric cross-field power input ($\bar{n}_c = 2.4 \times 10^{17}\,\mathrm{m}^{-3}$, $\tau_\perp = 3\,\mathrm{ms}$, $L = 15\,\mathrm{m}$). In contrast to Fig. 5, a poloidal grwoth of a marfe-type perturbation *without* relaxations is observed.

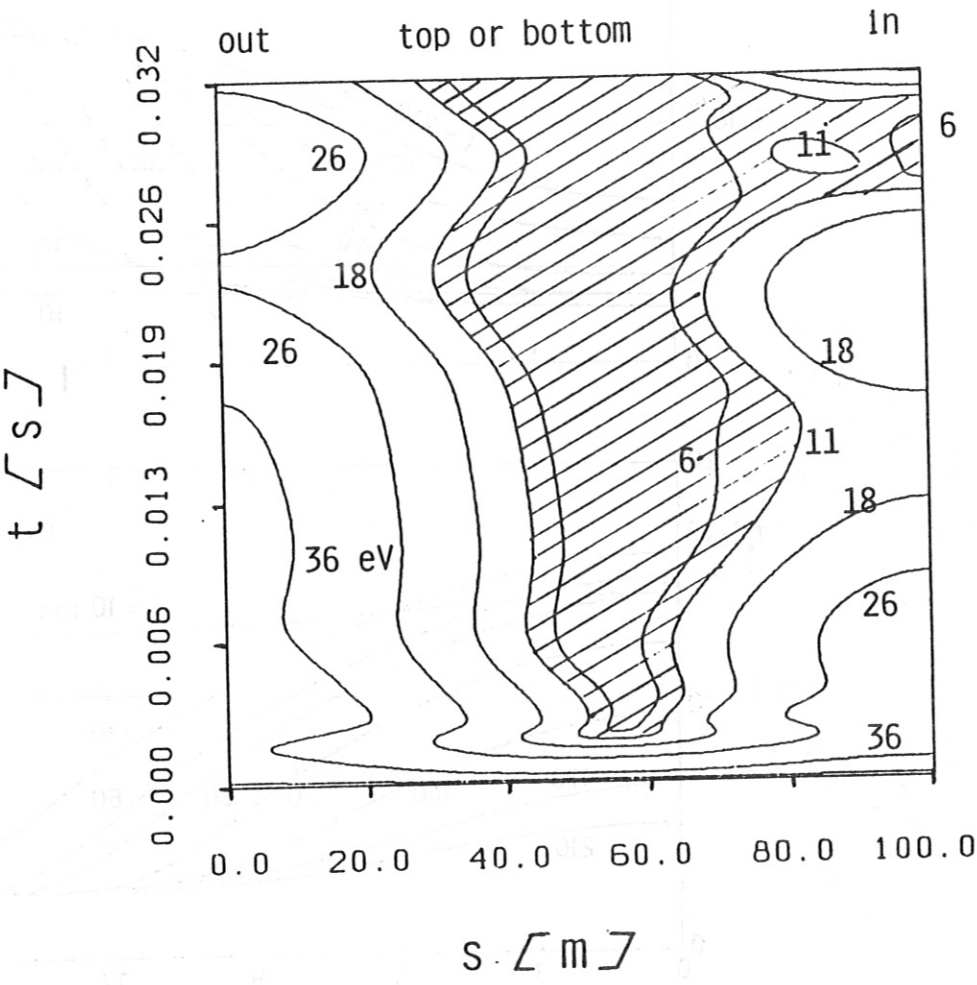

Fig. 11 A possible marfe history in the edge layer of a separatrix bounded elliptical plasma ($\alpha_1 = 0.2, \alpha_2 = 0.8$; see also Fig. 9) during density rise, taking properly into account the local perpendicular power influx. Lines of constant electron temperature are given in a (s,t)-plane. The shaded area corresponds to $T <$ 11 eV and indicates roughly the extension of the cool marfe region, forming at top/bottom with a tendency to coalesce at inside.

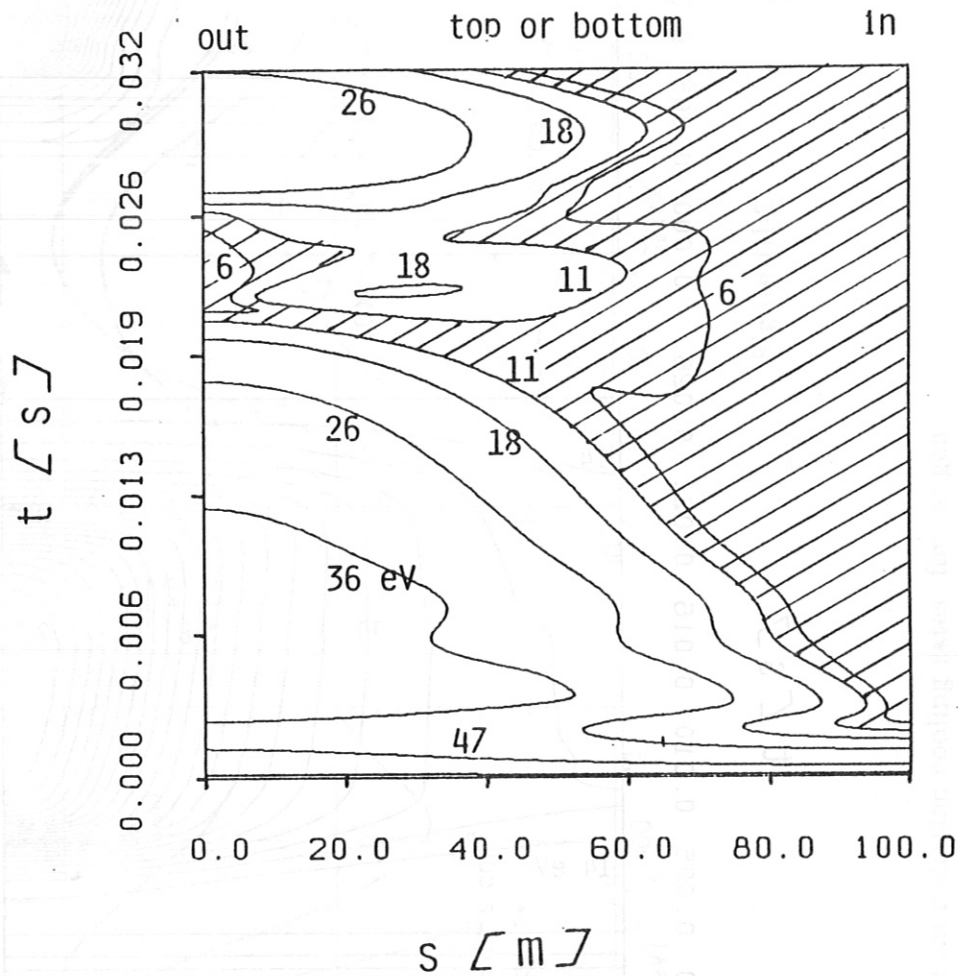

Fig. 12 Marfe history during density rise for in-out asymmetry of the local radial energy transport only ($\alpha_1 = 0.3, \alpha_2 = 0$) as appropriate for a circular cross-section. The shaded area again corresponds to $T_e < 11\,\mathrm{eV}$. A poloidally expanding standard marfe appears at inside as expected. As in Fig. 11, a quite realistic local power input model is used in contrast to previous examples and the average pressure on the flux bundle is no longer constant during density rise.

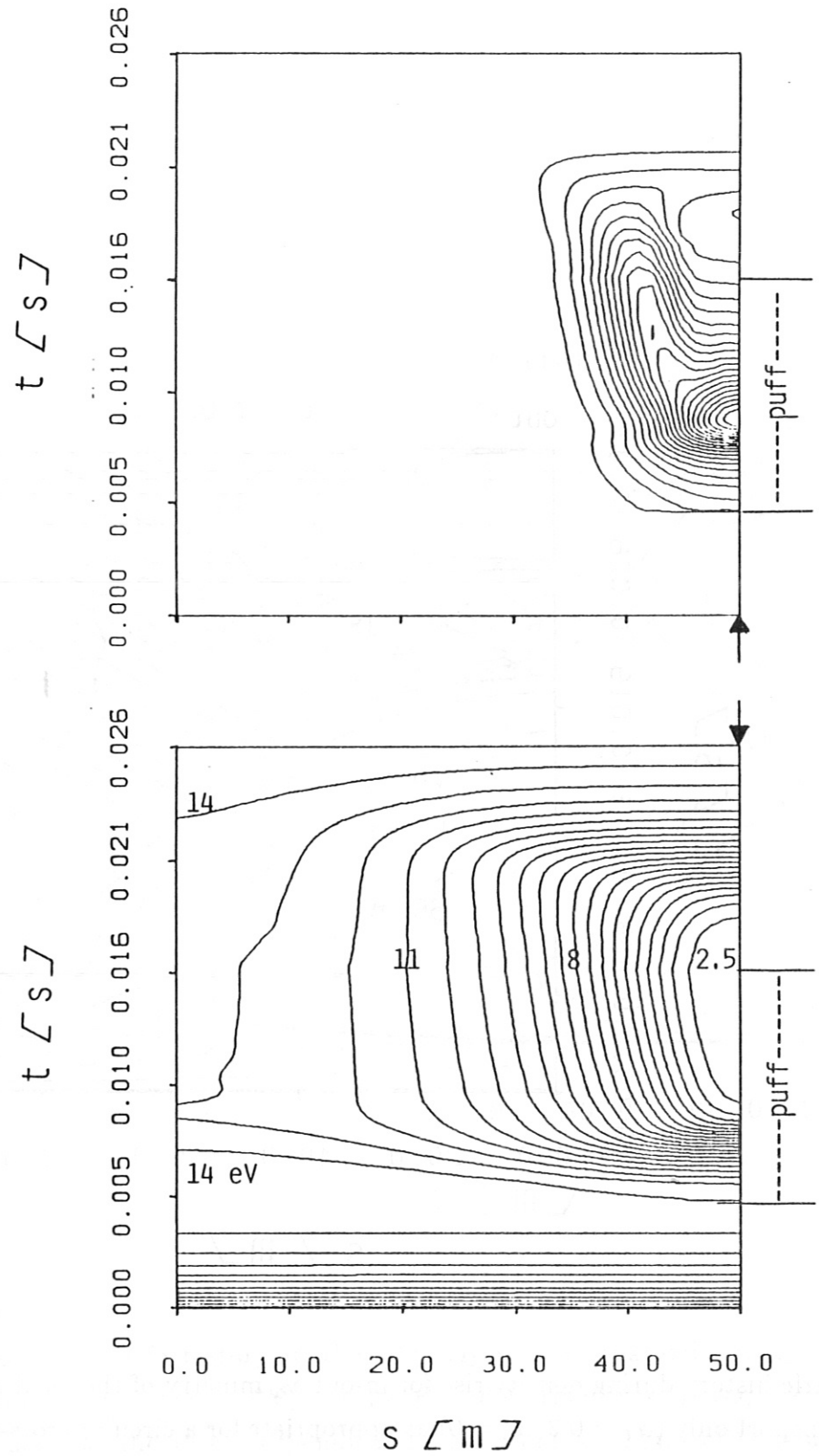

Fig. 13 A cool spot (local marfe) triggered by a 10 ms pulse of CII with a spatial decay length along field lines of 2m (e.g. methan puff, local carbon release, etc.). Lines of constant CIII density (top) and constant temperature (bottom; 0.62 eV steps) are shown in a (s,t)-plane. The pulse duration is indicated.

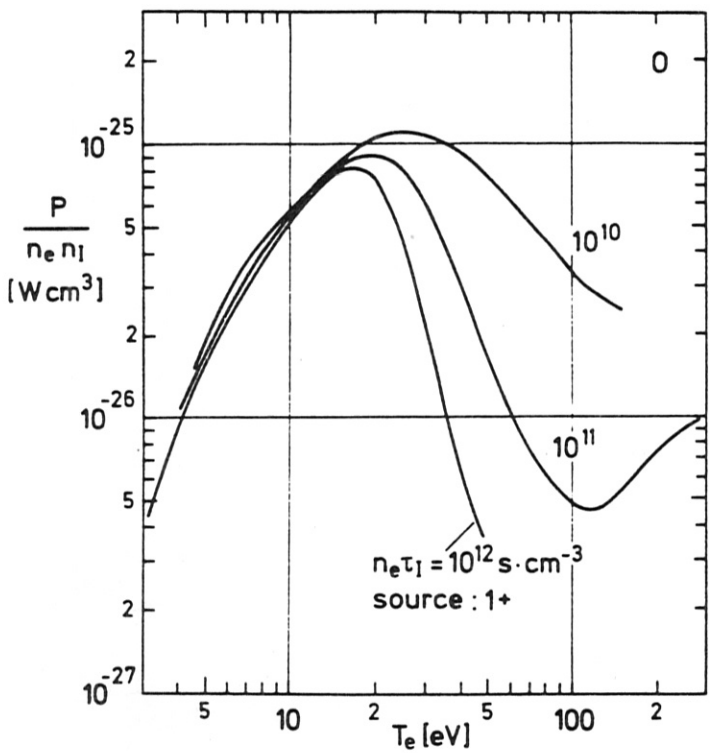

Figure III-1

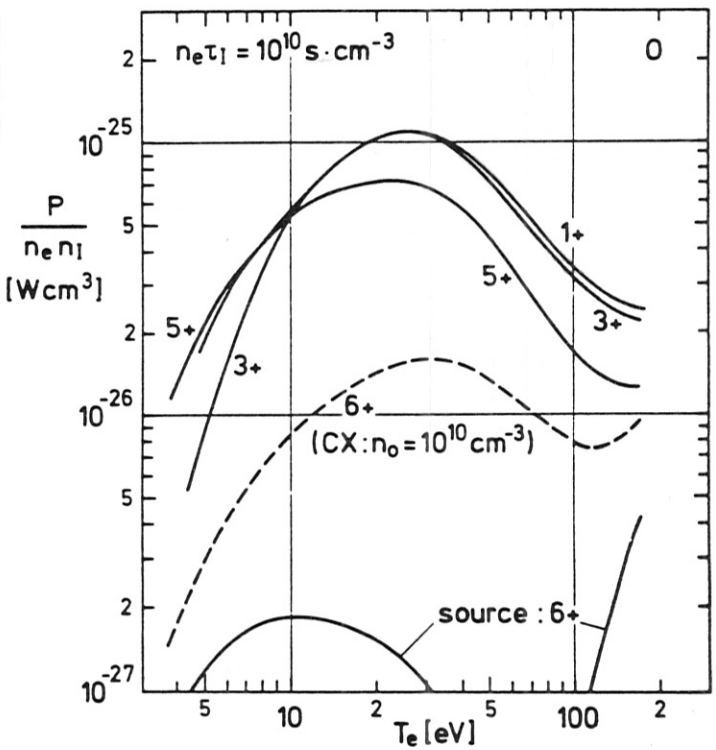

Figure III-2

Non-equilibirum radiation cooling rates for oxygen